3.C Hall C and the Super High Momentum Spectrometer (SHMS)

3.C.1 Overview

Much of the physics outlined in Chapter 2 can be accessed only by a spectrometer system providing key features not available in the existing CEBAF facilities. It must have acceptance for very forward-going particles and analyzing power for particle momenta approaching that of the incoming beam. It must provide excellent particle identification even at these high energies. It must be capable of rapid, accurate changes to the kinematic settings with well understood acceptances allowing experiments to efficiently cover broad regions of phase space, enabling, for example, precise L/T separations. The basic design must be flexible so that specialized detector elements, such as polarimetry or additional particle ID, can be incorporated to satisfy the needs of particular experiments. And it must possess an efficient, highly time-resolved trigger system and a target and data-acquisition system suitable for running at high luminosity.

Our plan for meeting these needs consists of producing a new Super-High-Momentum Spectrometer (SHMS) and outfitting the existing HMS spectrometer with a compatible data-acquisition system. The SHMS will be capable of analyzing the higher energy particles produced by the upgraded CEBAF beam at scattering angles as low as 4.5° (central axis at 5.5°). It will be designed as a companion to the HMS so that, taken together, the system will provide full momentum range single-arm capabilities as well as double-arm coverage over the entire kinematic region of interest to the proposed experiments. Thus, the SHMS will not be a replacement for the HMS, but rather a complementary partner to it just as the SOS (Short Orbit Spectrometer) functions as a partner to the HMS.

We present our plan by first reviewing the characteristics of the existing HMS in section 3.C.2. The physics demands developed in Chapter 2 of this report drive the proposed improvements to the HMS and determine the needed specifications for the companion SHMS. A summary of those specifications and a design for the SHMS which provides what the physics demands is given in section 3.C.3.

3.C.2 The High-Momentum Spectrometer

The HMS is a focusing spectrometer which can be tuned for central momenta from 0.4 to 7.3 GeV/c and production angles from 10.5 to 90 degrees relative to the beam direction. Its momentum acceptance is ±10% and the angular coverage is ±32 mr in-plane by ±85 mr out-of-plane, achieved by the optical system consisting of three quadrupoles in a FDF arrangement followed by a dipole. The angular acceptance is defined by a collimator near the upstream end of the spectrometer.

The optical system is followed by a detector stack made up of two pairs of crossed scintillator hodoscopes, twelve planes of precision drift chambers, a gas Čerenkov counter which can operate

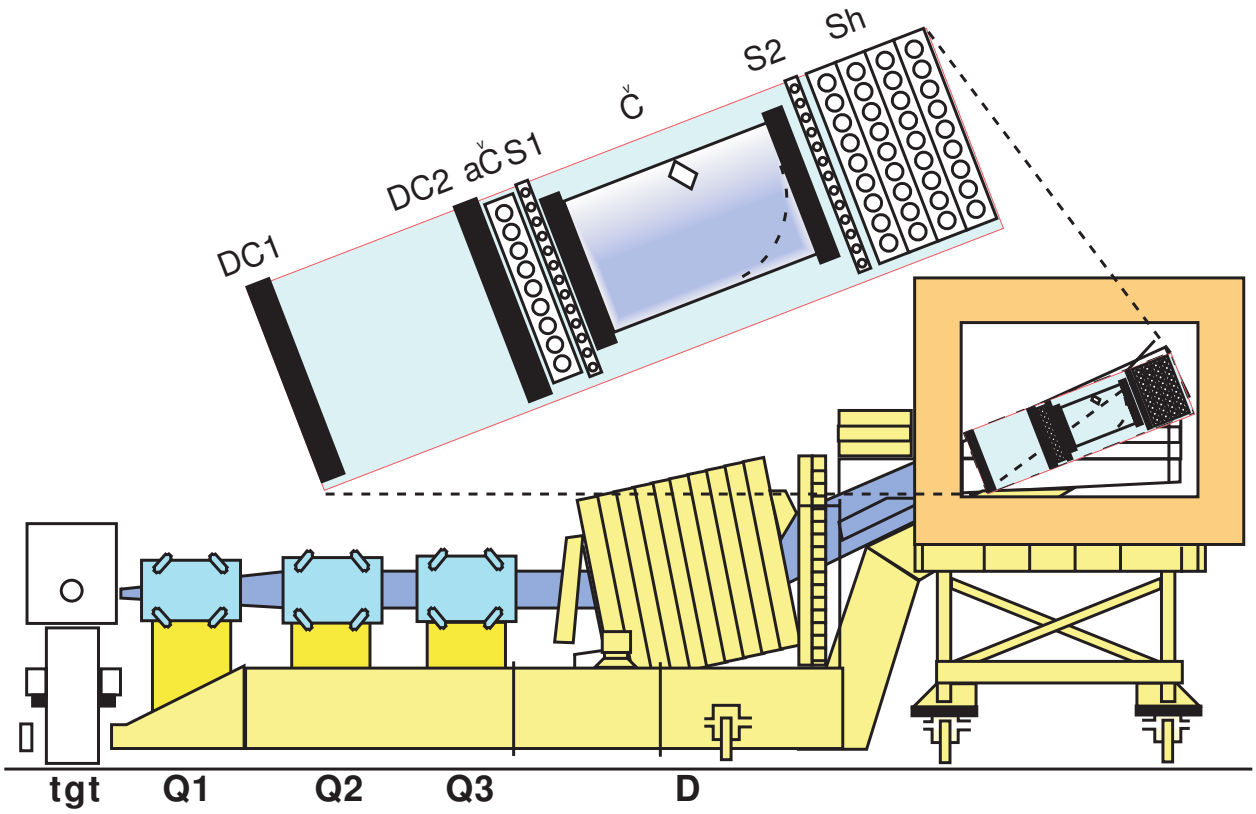

Figure 177: Sketch of the High-Momentum Spectrometer showing the Magnets, the Carriage, and an expanded block diagram of the Detector Stack.

from 0.3 to 2.5 atm., an aerogel Čerenkov counter, and a segmented lead-glass shower counter. A schematic diagram of the magnets and detector stack is shown in Fig. 177. The system is read out by a triggering and data-acquisition system providing full event readout of more than 2000 events/s with time-of-flight (TOF) and coincidence time resolution better than 200 ps.

Since the beginning of physics operation in Hall C, the HMS has provided precision tracking and particle identification for many experiments. Figure 178 shows some of the detector calibration results from these experiments which demonstrate its resolution and particle discrimination capabilities are summarized in Table 31.

Rotation of the whole spectrometer to the desired central scattering angle is accomplished remotely, without the need for access to the radiation enclosure, in about ten minutes. Angular setting accuracy is better than half a milliradian. Similarly, the central momentum may be adjusted remotely in about the same amount of time. These capabilities are crucial to experiments that must take data at a multitude of kinematic settings.

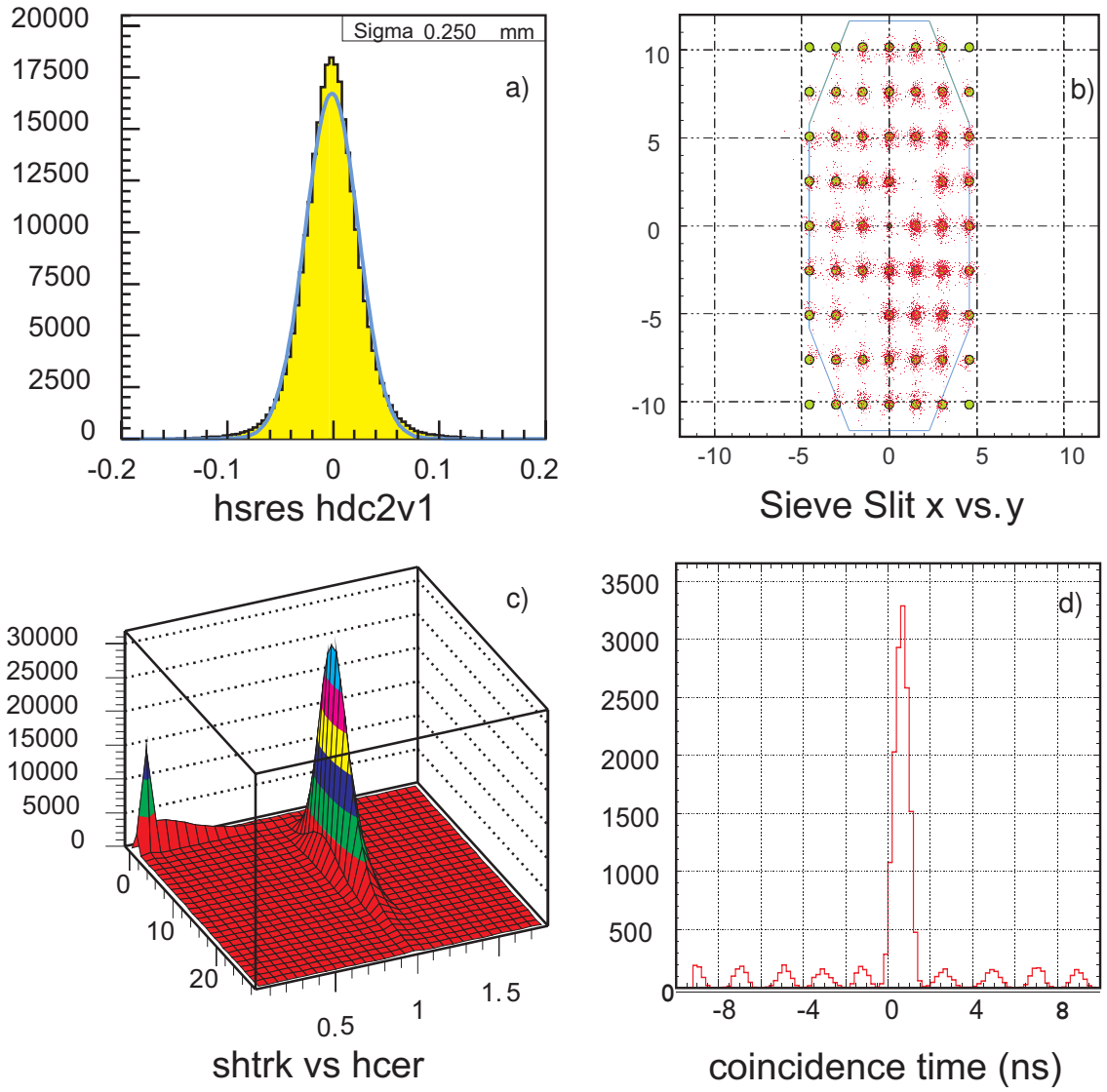

Figure 178: HMS Spectrometer Representative Data: Tracking capability is shown by a) Single-plane wire chamber resolution, and b) sieve slit reconstruction. Panel c) shows Shower Counter Energy vs. number of photons in the Čerenkov, demonstrating clear electron-hadron separation. Coincidence time resolution in the HMS–SOS hodoscope system is demonstrated in panel d) by the clear separation of particles from neighboring RF buckets.

Table 31: Summary of the HMS Performance and the Design Specifications for the SHMS.

Parameter	*HMS Performance*	*SHMS Specification*
Range of Central Momentum	0.4 to 7.3 GeV/c	2.5 to 11 GeV/c
Momentum Acceptance	±10%	-15% to +25%
Momentum Resolution	0.1% – 0.15%	< 0.2%
Scattering Angle Range	10.5 to 90 degrees	5.5 to 25 degrees
Target Length Accepted† at 90°	10 cm	50 cm
Horizontal Angle Acceptance	±32 mrad	±18 mrad
Vertical Angle Acceptance	±85 mrad	±50 mrad
Solid Angle Acceptance	8.1 msr	4 msr (LSA tune) 2 msr (SSA tune)
Horizontal Angle Resolution (yptar)	0.8 mrad	2-4 mrad
Vertical Angle Resolution (xptar)	1.0 mrad	1-2 mrad
Vertex Reconstruction Resolution (ytar)	0.3 cm	0.2 - 0.6 cm
Maximum DAQ Event Rate	2,000 events/second	10,000 events/second
Maximum Flux within Acceptance	∼ 5 MHz	∼ 5 MHz
e/h Discrimination	>1000:1 at 98% efficiency	1000:1 at 98% efficiency
π/K Discrimination	100:1 at 95% efficiency	100:1 at 95% efficiency

† This length corresponds to what the spectrometer can "see" perpendicular to its optic axis. The acceptable target length at any accessible scattering angle is, to first order, the projection of this length.

3.C.3 The Super-High-Momentum Spectrometer

Overview The Super-High-Momentum Spectrometer (SHMS) will play a vital role in the overall JLab physics program at 12 GeV. Short latency detector elements will minimize pileup and out-of-time events and, coupled with advanced data-acquisition components, will allow readout of 10,000 or more events per second. An inevitable consequence of relativistic kinematics is that much of the interesting physics at 12 GeV will only be accessible provided at least one of the spectrometers can achieve angles significantly below 10 degrees. The SHMS will achieve a minimum scattering angle of 5.5 degrees with acceptable solid angle and it will do so at high luminosity. The maximum momentum will be 11 GeV/c, well matched to the maximum beam energy available in Hall C. These three characteristics (high luminosity, small scattering angle, and high momentum) are essential for carrying out a program of electron-hadron coincidence experiments at large $z = E_h/\nu$, where ν is the electron energy loss. (For orientation, in the limit of $z \to 1$, one approaches the exclusive limit.) At large z (*i.e.* $z \approx 1$), sensitivity to the valence quark structure of the hadron is maximized and the reaction mechanism is simplified.

The HMS-SHMS spectrometer pair will be rigidly connected to a central pivot which permits both rapid, remote angle changes and reproducible rotation characteristics which simplify accurate measurements. From its inception, the SHMS momentum and target acceptances have been designed to be very flat, with performance similar to that of the HMS. This also simplifies making accurate measurements. These capabilities will facilitate experiments which rely on a large number of angle and momentum settings, such as L–T separations, for which accurate pointing as well as

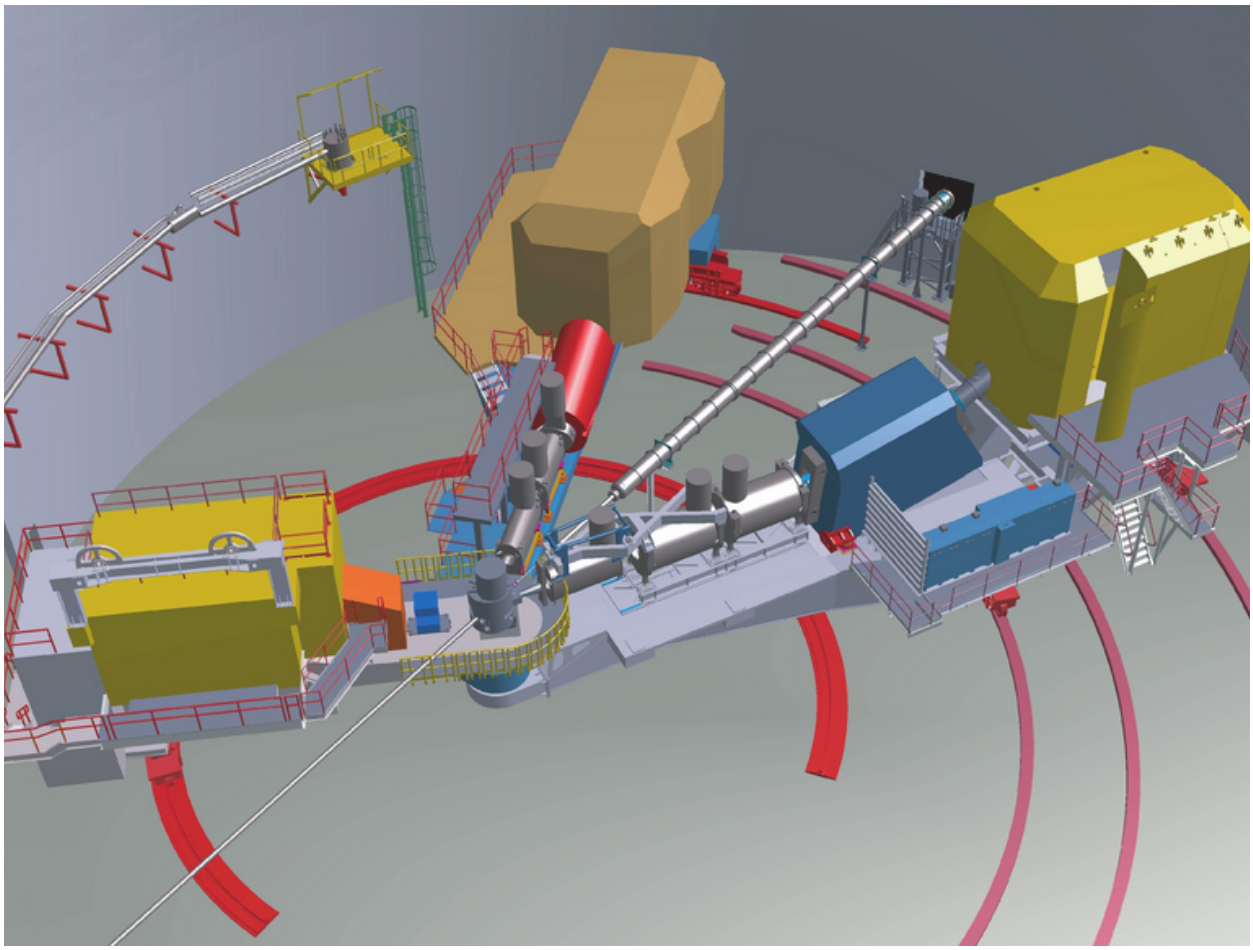

Figure 179: A CAD drawing of the new SHMS spectrometer installed in Hall C together with the existing HMS spectrometer (right) and the SOS spectrometer (left).

flat momentum and target acceptances are essential. Finally, for experiments which are willing to trade off small-angle performance for increased solid angle, this can be achieved by pulling the magnets and detectors forward and re-tuning the spectrometer. A CAD drawing of the new SHMS, together with the existing HMS and SOS spectrometers in Hall C, is shown in Fig. 179. In the remainder of this section we will address the design and performance details of the SHMS.

The SHMS Magnets and Structural Design

General The SHMS is an 11 GeV/c superconducting spectrometer. The magnet system consists of two cold iron quadrupoles similar in design to the HMS Q1, and a combined-function warm bore magnet that is 5 m long. The cryogenics are proven systems using standard JLab components. The shield house is a composite of concrete, steel and lead. The magnets and the

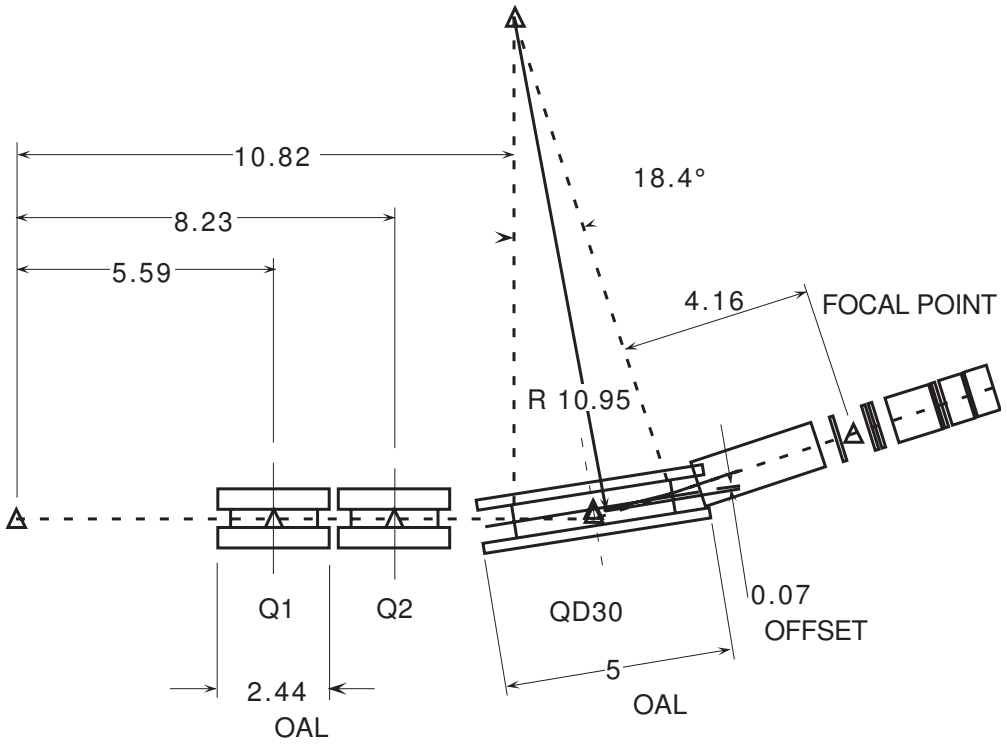

Figure 180: SHMS Spectrometer Key Dimensions (meters) showing the location of the two quadrupoles and the combined-function magnet relative to the target and the detector stack.

shield house are supported by a welded steel structure with steel drive wheels. Fig. 179 shows a perspective view of the spectrometer and Fig. 180 provides a line drawing of the layout.

Q1 at 8.6 T/m The SHMS spectrometer requires two quadrupoles with a gradient of 8.6 T/m and 40-cm aperture. The requirement to reach the scattering angle of 5.5 degrees means that the quads must be narrow. The existing HMS spectrometer Q1 magnet can just reach the required gradient due to the built in margin in operating current. The Q1 and Q2 magnets were designed by Oxford Instruments with a considerable operating margin so that the required gradients for HMS could be reached given some uncertainty in the yoke packing factor and the performance of the then new design of the large cold iron quads. The power supplies, for example, were sized at 1250 A even though the gradient was predicted to be reached at ∼1050 A. The cold iron quads worked as designed and the margin was never called into service. The margin in power supply current was matched by similar margins in the current leads, superconductor critical current, and force containment. Table 32 has the relevant Q1 parameters at the present maximum excitation and, for comparison, those required for SHMS. The forces at the 8.6-T/m gradient require further evaluation to determine if any internal structural modifications are required. The design margins in the present Q1 are very comfortable but much of this is lost at the higher excitation. Figures 181 and 182 show the gradient field quality and saturation at 8.6 T/m. Both are reasonable and meet the requirements.

Table 32: Q1 comparison between HMS at 1010 A and SHMS at 1291 A.

Parameter	HMS	SHMS	Change
Gradient (T/m)	7.11	8.59	20.8%
Current (A)	1010	1291	27.8%
Pole Tip Field (T)	1.78	2.15	20.8%
Field in Iron (T)	3.72	3.82	2.7%
Coil Forces†			
F_x (N)	28,571	44,062	54.2%
F_y (N)	7,465	-12,604	68.8%

†for Coil Stack 1

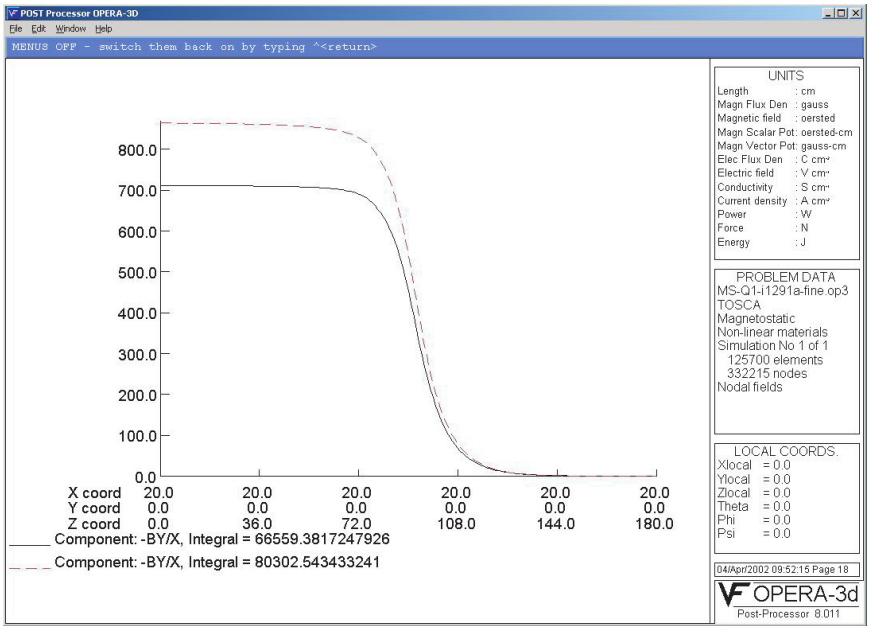

Figure 181: Comparison of the Q1 gradients along Z at 7.1 T/m and 8.6 T/m.

The project plan for SHMS is to procure, through competitive contracting, two Q1 magnet systems with a slightly thicker yoke shell to compensate for the ∼50% force increase. This modification will add a few centimeters to the overall size of the yoke/shell combination. The SHMS power supply will be rated for 1350 A, an increase of ∼10% over the present HMS Q1 supply. Similarly, the energy dump resistor will be designed to absorb a higher stored energy.

QD30 Superconducting Magnet for the SHMS The spectrometer requires a combined-function superconducting magnet that can simultaneously produce a 4.0-T dipole field and a 3.0 T/m quadrupole field inside a warm bore of 30 cm. A magnetic design using TOSCA 3-D[TOSCA] has been performed to establish the basic magnetic requirements, provide 3-D field maps for optics analysis, and produce basic engineering information about the magnets. A four sector cosine theta current distribution and a two sector cosine two-theta quad design with warm bore and warm iron has been selected and analyzed. A cut-away drawing is shown in Fig. 183.

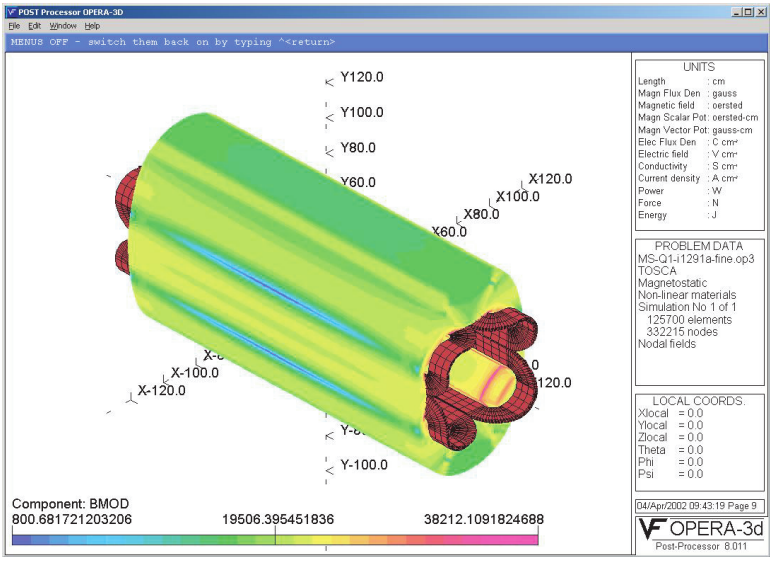

Figure 182: Magnetic Fields in Q1 at High Current.

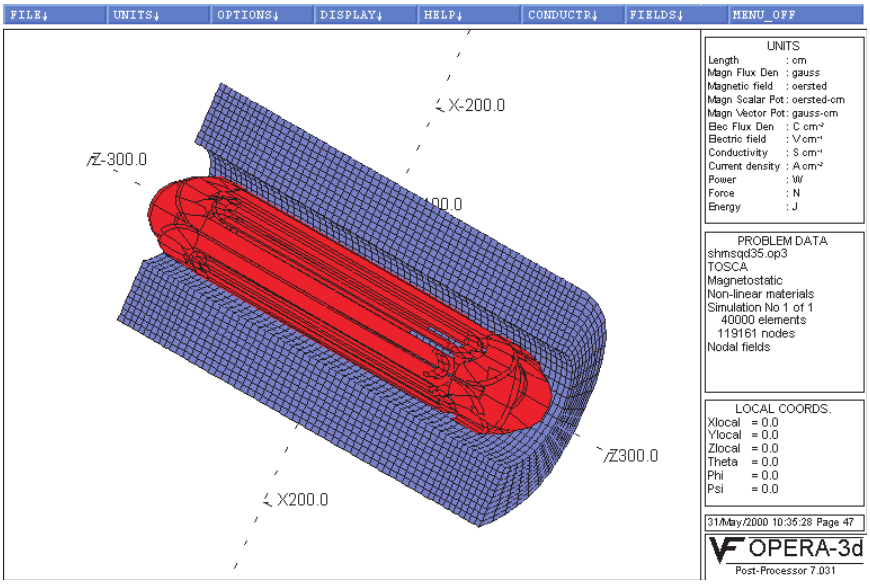

Figure 183: Cut-Away View of QD30 Magnet with beam–left side of yoke removed. Orientation is with bend field horizontal. Perspective angle is such as to make the image appear approximately as installed.

The magnetic design uses TOSCA-generated cosine theta type coils with "constant perimeter ends". These coils closely approximate the ideal cosine geometry that would be a perfect generator of high purity fields. Practical considerations such as finite current distributions, a limited number of sectors, and TOSCA's internal approximations, all contribute to deviations from the ideal geometry and are the sources of higher order field errors in the design. The yoke is modeled as non-linear iron with the nominal properties of 1010 steel. It is 4.2 m long with an outer elliptical shape having radii 120 cm 100 cm and a 60-cm inner circular radius. The detailed shape of the yoke is not very important in a cosine type magnet as the design requires an unsaturated yoke for good internal fields. The high field region is either on top or on the bottom depending on the relative sign of the dipole and quadrupole coils, therefore an elliptical yoke represents an ideal solution.

The QD30 combined-function magnet produces a peak field of 4.3-T in the bore and 5.4 T in the windings (see Figs. 184 – 187). These fields are comparable to those achieved in large bore magnets produced 20 years ago for MHD research, particle spectroscopy and coal sulphur separation. There are significant differences between the present magnet design and these prototypes. For example, the stored energy of the QD30 is somewhat less even though the field volumes are comparable. This is due to the fact that the superposed quadrupole field produces significantly less stored energy for a given maximum field. The combined fields also produce a very asymmetric resultant field and force distribution. The fields add on the bottom of the magnet and subtract on the top, so the fields across the bore range from ∼0 to ∼5 T. Similarly the fields in the windings are highest where the fields add (5.4 T) and nearly –2 T where they subtract. Thus there is a net force between the yoke and coil that must be dealt with due to the asymmetry. The peak linear force densities are 40,000 pounds per inch for the dipole winding and 11,000 pounds per inch for the quadrupole winding. These forces add on one side and subtract on the other yielding peak pressures that range from 4680 psi to 2100 psi. Simple pressure vessel computations for 20-ksi material stress yields a 6.0-inch thickness for the cold mass force collar. Due to the large radial thickness of the windings (3.5 inches) and cryostat (11.8 inches), the required 6-inch pressure shell is easily accommodated without stressing the coil cold mass. Obviously in a real cold mass the stress will be distributed and the resulting stresses lowered. The large size of the cryostat will allow separate fluid pressure vessels in accordance with the ASME code. This will greatly simplify the final design and result in a much more conservative magnet. A fully clamped winding is planned for the final construction.

Cryogenic stability of the QD30 quadrupole and dipole has been evaluated against the Steckly criterion, α. The condition of stability is that α must be less than one, which means that the velocity of spread of a normal zone is negative. That is, a normal zone will always shrink. Analysis shows that α is 0.79 and 0.48 for the dipole and quadrupole coil designs, respectively.

Magnet DC Power and Energy Dump System The DC power system for the SHMS magnets will consist of four independent power supplies. These supplies will be 12-pulse SCR supplies with a final stage transistor regulator providing stability of 10 ppm. They will be low-voltage high-current commercial units readily available from Danfysik and others. A DC current of

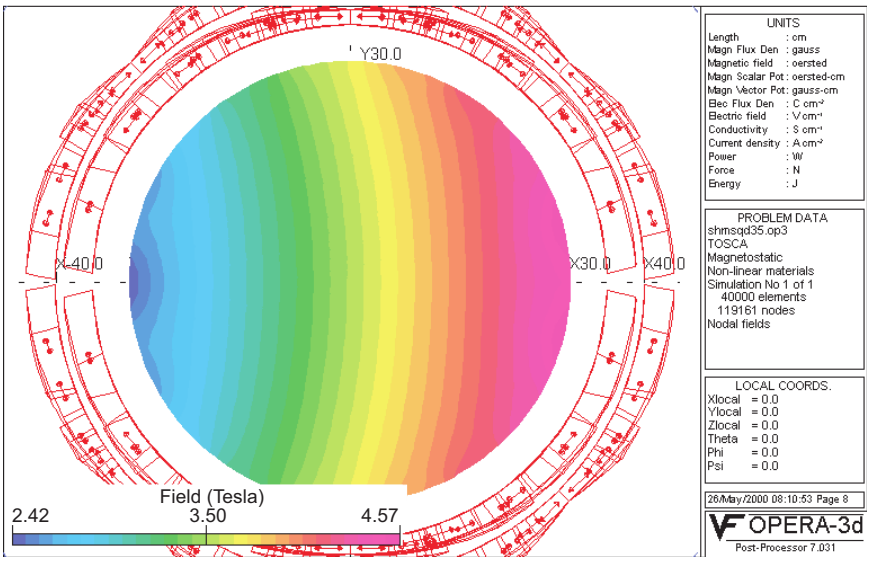

Figure 184: $|B|$ in QD30 Midplane (G).

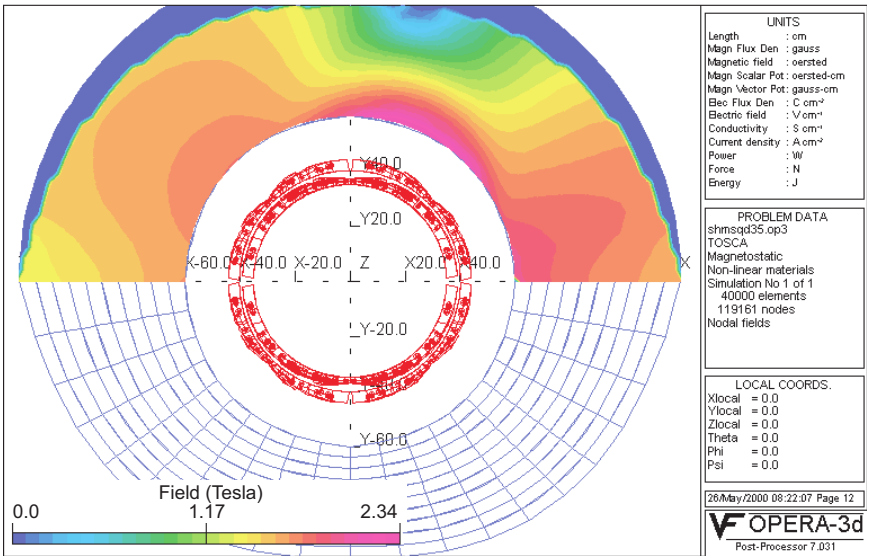

Figure 185: QD30 Yoke Saturation- $|B|$ (G).

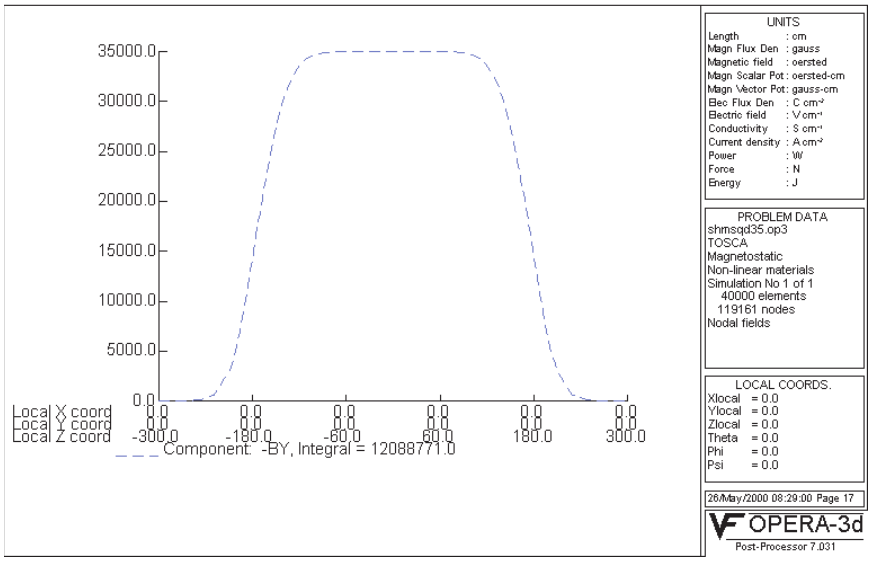

Figure 186: QD30 Dipole Field (B_y) along the central axis $x = y = 0$.

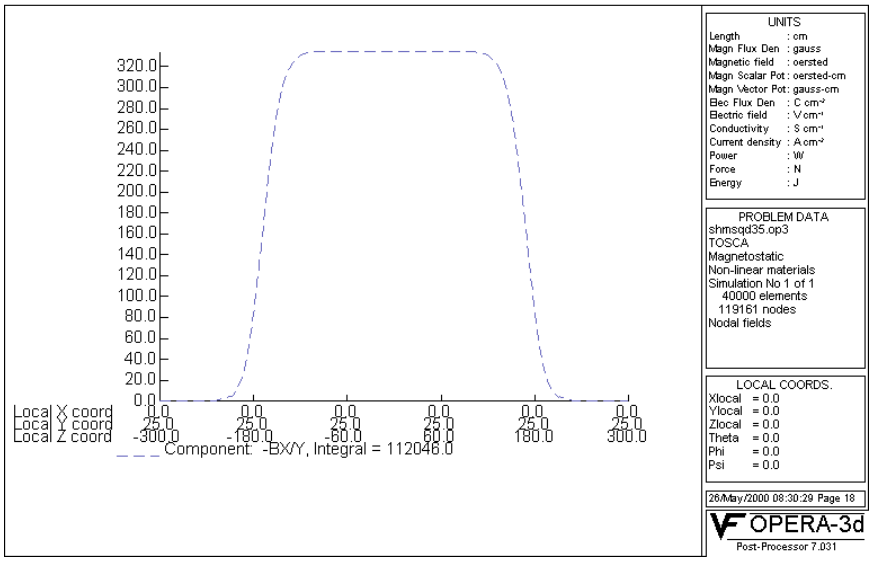

Figure 187: QD30 Field Gradient $\partial B_x/\partial y$ along $x = 0, y = 25$.

Table 33: SHMS QD30 Magnet Parameters.

Function	Combined Quadrupole – Dipole	
Bore	30 cm Warm	
Overall Length	5.0 m	
Outer Diameter	3.2 m	
Yoke	240 kilopound (kip) warm 1010 steel. Length: 4.2 m.	
	Outer envelope: ellipse with half-axes 1.2 m $\times$ 1.0 m.	
	Inner envelope: 0.6 m radius circle.	
Coil and cryostat	40 kip St.Steel 5 m Long, 0.6 m (0.3 m) outer (inner) radius	
Stored Energy	13.0 MJ	
	Dipole	Quadrupole
Amp–Turns	3.3×10^6	1.8×10^6
Current Density	$5600 A/cm^2$	$5040 A/cm^2$
Coil Sectors	4	2
Winding	cosine(θ)	cosine(2θ)
Magnetic Strength	12.50 Tm	11.48 (T/m)m
Central	Field 3.58 T	Gradient: 3.63 T/m
Effective Length	3.45 m	3.4 m
Uniformity	dB/B $\sim 1 \times 10^{-3}$	dG/G $\sim 1 \times 10^{-3}$
Peak force density	40 kip/in	11 kip/in
Peak pressure	3390 psi	1290 psi

5000 A at 10 V would be a reasonable choice for SHMS dipole due to the relatively low inductance (0.72 H), and would provide a charge time under 30 minutes. The Quad power supplies will be identical to those in use on HMSQ1 and the QD30 magnet supply will be similar to the new HMS dipole power supply. All of the supplies will provide $\sim$ 10 V for ramp-up or ramp-down, have polarity reversal switches, and the possibility of NMR control for the dipole coils.

The energy dump systems will consist of a 10 V ramp-down, a slow dump and a fast dump resistor. The fast dump for the Quads will provide 450 V while the fast dumps for the QD30 magnet will apply a voltage of 150 V to the dipole coils and 250 V to the quad coils. These voltages may increase as the design progresses to maintain a reasonable final coil temperature near 80 K. The large cold mass and moderate current densities ensure that sufficient material is available to absorb a large fraction of the stored energy at a low final temperature during a quench discharge. The QD30 magnet circuits will have dump resistances such that the time constants are equal so that both coils will discharge at the same rate. The design is such that in the event of a discharge of one coil set, the second set will see a voltage which mimics a quench and a discharge of the second coil will be initiated. The possibility of a real second coil quench is also likely due to eddy current heating in the stabilizer material.

Magnet Control System The SHMS magnets will have a control system that is self contained and able to be operated remotely by EPICS. The magnets' internal controls will take care of interlocks, operating valves by PID, and converting information from the magnet into

engineering units. The EPICS system will allow operation from remote screens, archival data logging and graphic display. A dual processor PLC designed for critical fail safe process control will be used. Such PLCs can switch the process control from primary to secondary in ∼50 ms in the event that the primary processor fails. They can also be switched manually or by software for routine maintenance. The use of dual processor PLCs can reduce if not eliminate the nuisance of radiation induced local processor lockup. The PLC will use a combination of commercial electronics and PLC I/O modules for signal acquisition. Liquid level control and cryogenic thermometry is straightforward to provide using commercially available units. Readouts of magnet voltages, pressures, strain gauges and valve position LVDTs will be performed by standard PLC plug–ins.

Support Structure The SHMS support structure will be a welded steel frame riding on steel wheels and a center bearing. The structure will be built from prefabricated sections that must be welded together in the Hall. The steel structure will have a main beam section that will carry the entire spectrometer. The entire beam and spectrometer will ride on large hinged steel wheel bogies and floor mounted rails to allow precise scattering angle changes. This system is similar to that used in the HMS and SOS spectrometers. The steel fabrications will be hollow welded structures similar to ship hull sections. As such they will have internal access to permit complete welding of all seams and joints. The wheel sections will be driven by motors and reducers with variable frequency drives. The wheels are planned to be conical sections that are machined at the proper angle to control the radius of rotation. The use of the successful "Bertozzi" hinges on the wheel assemblies to eliminate the large radial forces that arise from even small misalignments is incorporated in the design.

Spectrometer Motion System The SHMS spectrometer has a required range of motion from 5.5 degrees to 25 degrees. These two orientations are shown in Fig. 190. Proximity detectors will ensure that the system always moves in a safe angular range and that obstacles are avoided. Positioning accuracy consists of three components: angular measurement, pointing control, and distance from pivot. The scattering angle positioning tolerance will be 0.01 degrees, the pointing tolerance will be ±0.5 mm, and the distance off the pivot will be constant to within ±1 mm. While it may be possible to measure these quantities more accurately, these are the spectrometer setting tolerances. Note that this is similar to what has been obtained with the HMS. The scattering angle will be measured by a shaft encoder that can detect an angle change of 0.003 degrees. A scale etched into the floor at the radius of the rear drive wheels and viewed by a video camera with a graticule lens will confirm the scattering angle setting. Pointing and distance from pivot will be controlled by a large central crossed roller bearing. The accuracy of such bearings is a few thousandths of an inch. A view of the pivot showing simultaneous connection of the SHMS, and SOS, and the HMS, is provided in Fig. 189.

The motion of the SHMS spectrometer will be coordinated by a stand-alone PLC that integrates the drive wheel motion, angle read-back, proximity sensors, and obstacle detection. The

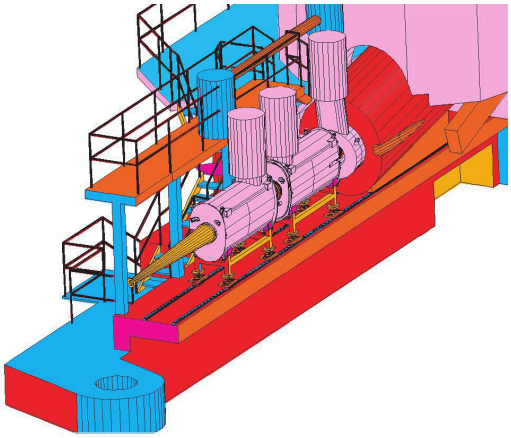

Figure 188: SHMS Pivot with Slider.

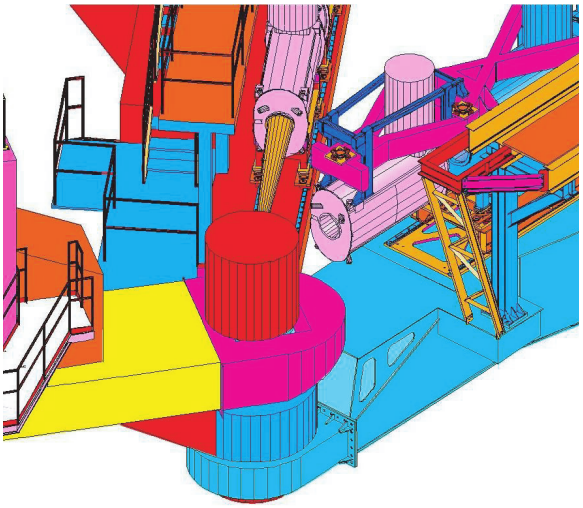

Figure 189: Hall C Pivot with (from left) SOS, SHMS, and HMS Attached.

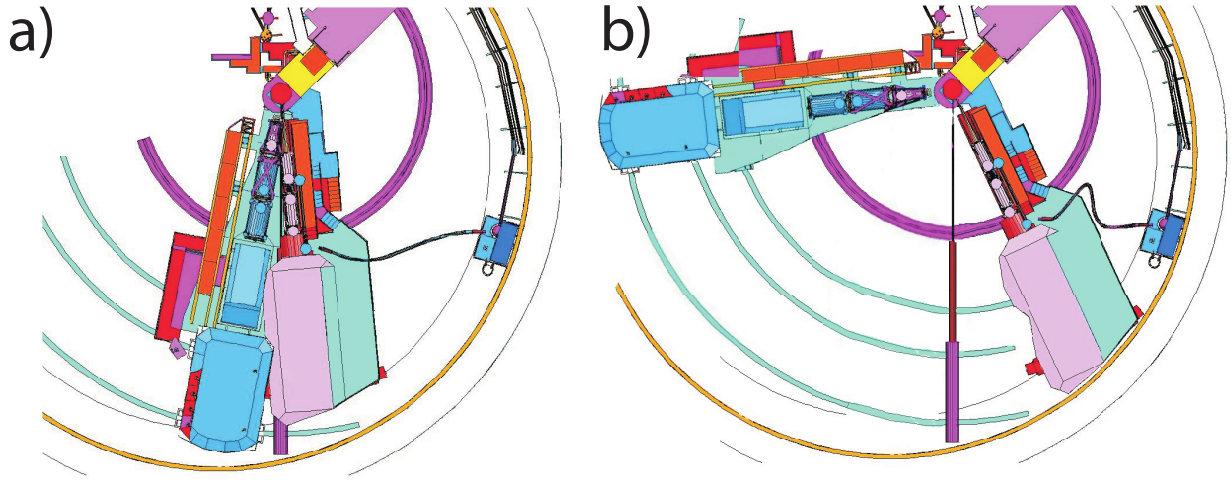

Figure 190: The SHMS-HMS spectrometer pair in two extreme configurations: a)the SHMS at 5.5° and the HMS at 10.5° ; and b) the SHMS at 25° and HMS at 85°.

rotation motion will be limited to a preprogrammed range set in EPROM in the PLC and by the proximity detection. This design is similar to the HMS rotation control system.

Shield House The SHMS spectrometer shield house will be a reinforced cast concrete structure that is built on the steel carriage. The concrete thickness will be 100 cm on all sides except toward the pivot where it will be 200 cm. The concrete is formed and poured in place. A conventional concrete mix will be used with added borate to absorb thermal neutrons. The interior walls, floor and ceiling will have a minimum 2-inch thick lead lining except for the front wall which will have 3 inches of lead. The lead will be covered and constrained by a system of aluminum plates and C channels. The SHMS detectors will be mounted on a transverse rail system so that the detectors may be easily removed for servicing and relocated accurately. The shield house will be accessed by a door that is hinged to open outward on the side away from the beam, and a removable block wall. There will be a limited amount of space inside the shield to allow a corridor access on both sides of the detector stack.

SHMS Cryogenic System

Description The SHMS magnets will be designed with a cryogenic interface similar to the existing HMS magnets. Internally the magnets will have thermal siphon circulation from helium and nitrogen reservoirs. The reservoirs will contain dual relief devices: an ASME coded mechanical relief and a rupture disc set at a 25% higher pressure. Exhaust lines for relief which are separate from the cool-down lines will be used so that there will be no chance of a contamination blockage in these pressure relief paths. Temperature sensors, liquid level sensors, and voltage taps will be within the reservoirs. The magnets will have liquid level control and valves to permit independent

warm up or cool down using a local heat exchanger. The cryogenic valving will allow for top-fill and bottom-fill of helium and nitrogen for steady operation and for cool-down, respectively. Cold return and warm return shutoff valves will be included to allow a smooth transition from cool-down to regular closed cycle operation. The cryogenic supply will use the existing Hall C G0 transfer line including the G0 flex line, vacuum jacketed return lines, flex gas lines and cool-down heat exchanger. The SHMS cryogenic system will use a new cryogenic distribution box mounted on the back of SHMS and a flexible transfer line similar to that constructed for the G0 experiment. The magnets will be connected by JLab standard U-tubes similar to those used on HMS/HRS quads. A set of gas manifolds installed on the back of the SHMS will collect and return cryogenic gases to the existing Hall C cryogenics system. A stand and a platform are required for support of equipment and for personnel access. The system is completed by automated cool-down valves and actuators identical to those used on HMS.

Operating modes During normal operation the SHMS magnets will be fed helium gas at 4.5 K and 3 atm. This gas gets JT expanded at each magnet by a valve that is controlled by the SHMS magnet control system to maintain liquid level. Boil off gas and JT flash will be returned to the local refrigerator at 1.2 atm. and 4.2 K. Nitrogen will be fed to the SHMS at ∼85 K and 4 atm. where it is expanded into the N_2 reservoir by a valve under local control. Boil off N_2 will be vented outside. Vapor cooled current leads will be controlled by valves that servo on the SHMS magnet current and adjust the helium gas flow accordingly. Separate flow control and measurement for each current lead is a normal part of this design. Non burn-out current leads are specified. The helium gas from the leads will be returned warm to the End Station Refrigerator compressor suction. The cool-down gas return and N_2 gas return lines will be vacuum jacketed to prevent ice and water from accumulating near the magnets.

Internally the SHMS magnets use thermal siphon circulation. An insulated supply line will feed helium to the bottom of the magnet cryostat and a return line will collect the slightly less dense fluid at the top of the cryostat and return it to the helium reservoir through a stand-pipe. The magnet heat leak will provide the energy to drive the circulation. The pipes are sized for 10 times the design heat load to ensure stable thermal siphon flow under all conceivable conditions. The LN_2 system design is similar.

During cool down and warm up, 4-atm. helium gas at 300 K will be blended with a pre-cooled 80-K helium stream on the SHMS in a "cool-down heat exchanger" (CDHXR). This variable temperature source will be controlled by the SHMS magnet control system to provide a 70-K differential temperature for either warming or cooling, and will maintain an internal temperature difference in the SHMS magnet of no more than 50 K. This CDHXR will provide a precise method of warming and cooling the SHMS magnets independently in a manner which minimizes thermal stress due to relative contraction. This technique will also provide increased cryogenic efficiency.

SHMS Vacuum Systems The SHMS spectrometer will have three vacuum systems dedicated to the operation of a) the QD30 superconducting magnet, b) the SHMS spectrometer vacuum, and c) the Čerenkov detector. The SHMS cryogenic system is presumed to be made leak tight and cryo-pumping so a dedicated vacuum system is not included in the design. The QD30 magnet will also be leak tight, but a vacuum system tailored to leak testing, commissioning and biannual vacuum servicing will be included as a dedicated system. It can be used to commission and service the cryogenic system as needed. It will be portable, self contained, and fully instrumented. The spectrometer and Čerenkov vacuum systems will be dedicated to those devices and will be permanently installed on the SHMS.

The pumping system for the QD30 magnet will consist of a turbo pump backed by a direct drive roughing pump. A 1000 liter per second turbo pump with a full port gate valve, roughing bypass manifold and leak testing manifold will be required. The wheeled pump station will have a mechanical $30 - 0 - 30$ vacuum gauge, high range and low-range thermocouple gauges, and a cold cathode ion gauge. A dedicated RGA for system commissioning will be needed. A large full port cold trap that can be piped in for system startup and mounted on a separate wheeled cart is included in the specification. Appropriate auxiliary vacuum hoses, valves and flanges to facilitate connecting to all the SHMS vacuum systems will be provided as well.

The SHMS will have thin aluminum entrance and exit windows. The windows will be hydroformed spherical shapes similar to those in use on the HMS. The spectrometer vacuum between these windows will be maintained by a large mechanical pump and roots blower as a roughing system, and a 1000 l/s turbo pump.

The Čerenkov vacuum and gas system design is similar to the above but includes the capability of introducing other gases besides helium. This system will be dedicated to providing the correct Čerenkov atmosphere and will have differential pressure relief valves to limit the operating pressure range. Appropriate monitoring equipment to verify that the correct index has been achieved will be necessary. An arc cell system and a hygrometer will be used for quality control of the process. The Čerenkov system operates first with a nitrogen purge to dry the system, then the nitrogen is displaced with the detection gas. A small volume purge of the detection gas may be maintained to permit monitoring of gas quality.

SHMS Optics and Monte Carlo

SHMS Optics Design The goal of the SHMS design was a compact, general purpose spectrometer similar in properties to the HMS, but with a higher maximum momentum setting for experiments that will use the 11 GeV beam available in Hall C from the CEBAF upgrade. The SHMS needs to be compact in order to fit into the forward-angle space now used by the SOS spectrometer, with angular range from 5.5 to 25 degrees, and a minimum angle with respect to the

HMS of 16 degrees. The design process also sought to minimize the cost. A summary of the design parameters is given in Table 31.

To achieve these goals, the SHMS was designed as a vertical bend, QQ(QD) spectrometer. Two quadrupole magnets are followed by a combined-function magnet that includes both quadrupole and dipole elements. This is similar to the HMS optical layout, except that the last quad and the dipole have been superimposed to make the spectrometer compact.

The first two quads are copies of the HMS Q1 magnet. Re-use of this design helps keep costs low, and the performance of these magnets is well known. The QD is a new design, the engineering details of which may be found in section 3.C.3. Because of the large fields required to bend 11 GeV electrons in a compact spectrometer, the QD must be superconducting, without iron pole-faces. The coils are enclosed in a cylindrical shell of iron, which serves as a flux return yoke. This configuration is very compact, and relatively inexpensive to build. However, it is not a true QD magnet. That would require a toroidal iron shell, and similarly curved coils. A true QD magnet would be very expensive to build, and the performance of the SHMS with a cylindrical QD is adequate.

The SHMS design is very flexible. The coils in the QD are separately excited, and the magnets and detectors will have adjustable positions, making many tunes possible. We consider two here: the original Small Solid Angle (SSA) tune used to design the spectrometer, and a Large Solid Angle (LSA) tune, with all magnets and detectors moved forward 2.32 meters as a rigid body.

Several tools were used in designing the SSA tune. The first of these is TOSCA[TOSCA], a finite-element, 3-D magnetostatics program. The results discussed here come from the 'QD30' TOSCA model of June 5, 2000. TOSCA calculated the field values on a 3-D grid inside the magnet, and a model was fit to the horizontal, or y field component on the $y = 0$ plane (the vertical mid-plane, or symmetry plane of the magnet.) A ray-tracing program was then used to numerically integrate the equations of motion for an electron in the model's field. This determines the trajectory of the central ray in the spectrometer.

Early in the design process, the total bend angle was fixed at 18.4 degrees. This is essentially the maximum that can be allowed without limiting the acceptance through the QD magnet. An important point to realize is that the quadrupole fields in the QD bend the central ray. Optimizing the spectrometer performance involved tuning the Q/D ratio, and this required compensatory changes in the dipole strength in order to preserve the correct bend angle.

It should also be noted that the central ray has to be offset from the exact center of the QD to avoid cutting off the acceptance by the magnet entrance and exit. Monte Carlo simulations showed that an offset of 7 cm in the center of the magnet combined with a beam-pipe transition at 200 cm from the QD center would optimize the acceptance. This layout is shown in Fig. 180. A complex transition pipe will join the QD to the neighboring quad magnet.

With a central trajectory specified through the QD, the optics of the spectrometer as a whole could be studied. The optics are defined by map functions that transform the trajectory of a particle at one location to its trajectory at a different location. We used the COSY [COSY] program to calculate 5th order Taylor series polynomial expansions of both the global map from target to detectors, and the individual sequential maps that transform from one significant aperture in the spectrometer to the next. The COSY calculations are based on a model of the spectrometer magnets that we describe below. Concurrent with the map calculations, COSY would track an ensemble of test rays through the spectrometer, and adjust the strength of the first two quads to produce the sharpest focus at the detectors. This process was iterated with manual adjustment of other parameters, such as focal plane position, to optimize the performance. The end result was the standard tune. Parameters of the standard tune are given in table 34, and the tracks of 27 test rays are shown in Fig. 191.

COSY magnet model Standard COSY quadrupole elements were used for the two quad magnets, as was done in the HMS optics model. There are no COSY standard elements corresponding to the QD magnet, and it had to be modeled using the general field-map element. Past experience has shown that this requires extremely smooth field-map data, such that the TOSCA field-maps could not be directly used. Instead, field values were calculated from a model fit to the data. The use of a model also allows changes to be made in the fields to simulate small changes in the dipole and quadrupole coil excitations for tuning purposes. This model was also used in the central-ray integrations mentioned above. The form of the model is:

$$B_y(x,z) = \sum_{i=0}^{6} C_i(z)\,(x/r_0)^i \tag{75}$$

in which (x, y, z) are right-handed Cartesian coordinates with z the axis of the magnet pointing downstream, y is horizontal, and x is in the vertical plane, pointing upwards, with origin the center of the magnet; B_y is the y-component of the magnetic field in the plane $y = 0$; and $r_0 = 30$ cm is the radius of the beam-pipe. For each discrete z_j in the TOSCA data, polynomial coefficients C_{ij}^T were fit to the data using the method of singular value decomposition. Gaussian interpolation was then used to calculate coefficients at arbitrary z:

$$C_i(z) = \sum_j C_{ij}^T \,\exp(-[(z - z_j)/(s\,\Delta z)]^2)/(s\,\sqrt{\pi}) \tag{76}$$

where Δz is the 2-cm grid spacing. $S = 2.5$ gives smooth results that accurately reproduce the TOSCA data.

As mentioned above, both the dipole and quadrupole coil excitations needed to be adjusted by small amounts to fine tune the bend angle and optimize the focus. In principle, this could be done by re-running the TOSCA model, but this was not practical. Instead, we use symmetry arguments

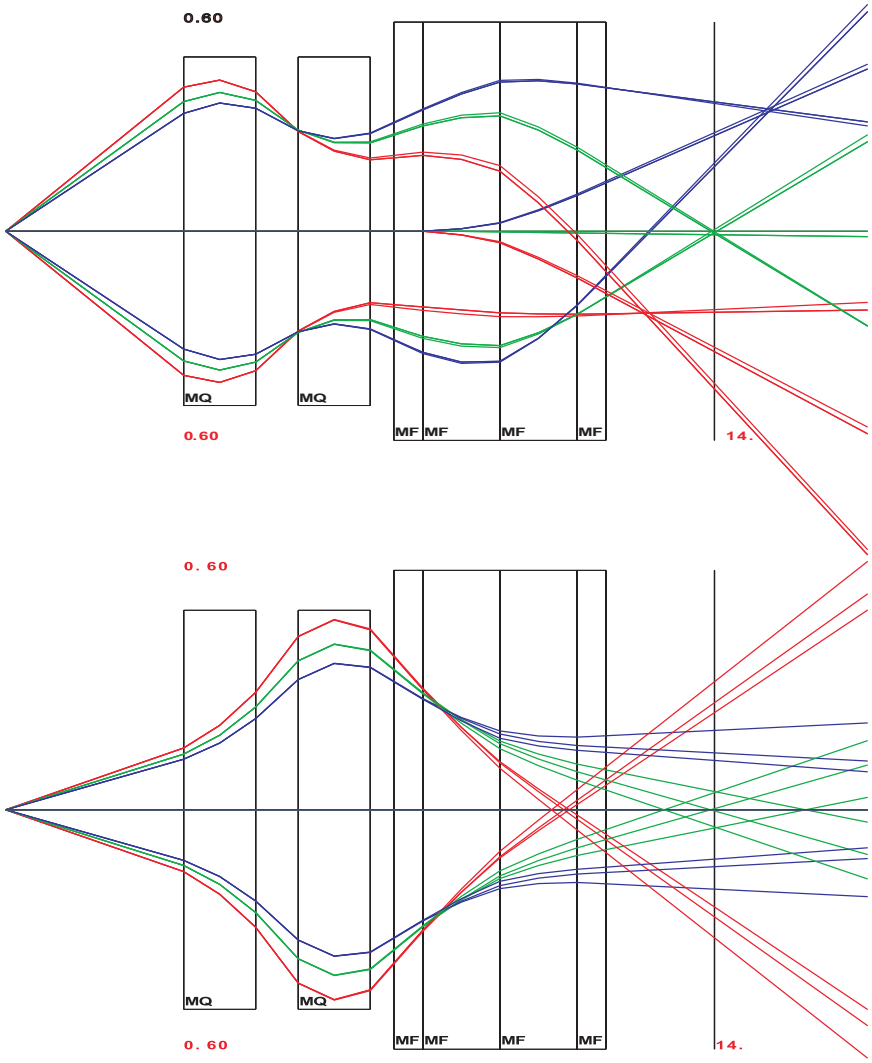

Figure 191: Rays Tracked through the SHMS by COSY for the SSA Tune. The top panel is the bend-plane projection (COSY (x, z) coordinates), while on the bottom is the transverse projection (COSY (y, z) coordinates). 27 rays are plotted for all combinations of 3 values of total momenta ($\Delta p/p_0$ = 0.1 [blue], 0 [green], -0.1 [red]), 3 values of p_x/p_0 (0.4, 0, -0.4), and 3 values of p_y/p_0 (0.15, 0, -0.15).

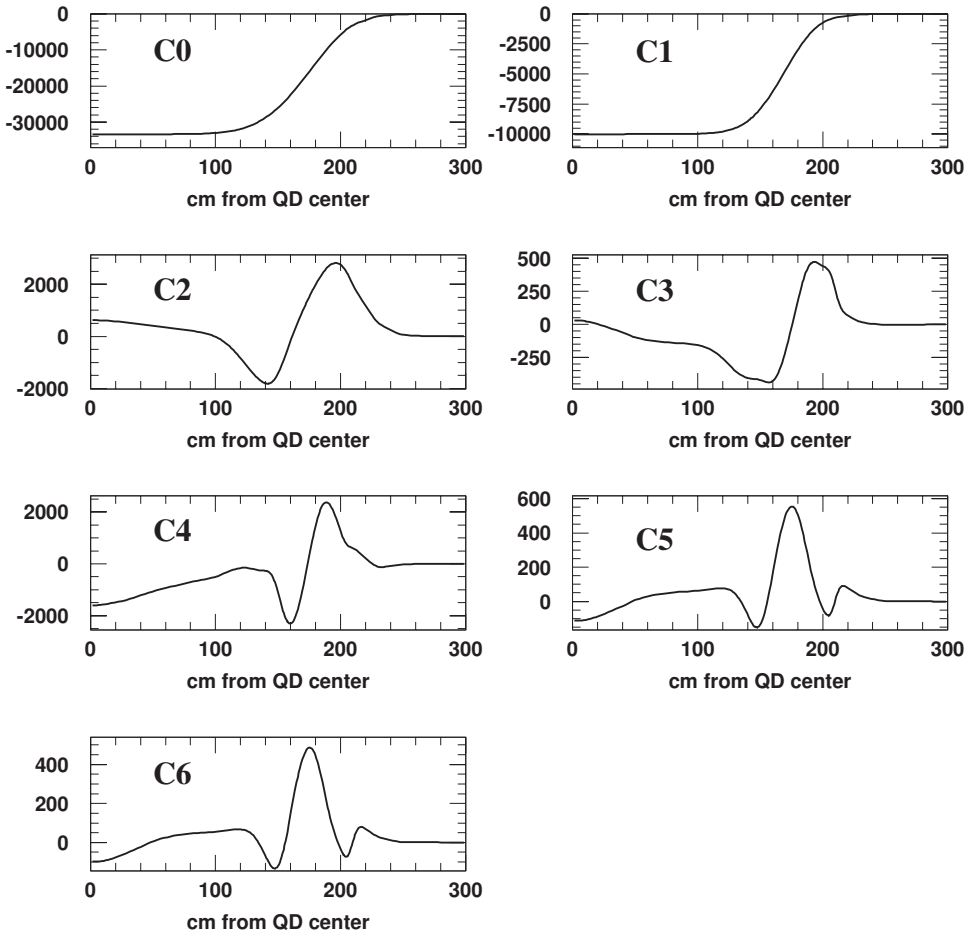

Figure 192: Polynomial Coefficients in the QD Magnetic Field Model as a function of z, the axial distance from the magnet center. (The functions are symmetric about $z = 0$.) $C0$ is the dipole component, $C1$ the quadrupole component, and the others are higher order contributions. The vertical axes are the contribution to B_y at $x = 30$ cm, in gauss.

to treat all the terms in the model that are even-order in x as harmonics of the dipole coils, and the others as harmonics of the quad coils. Thus, we adjusted the dipole excitation in the model by simply scaling the even-order coefficients, and similarly adjust the quadrupole excitation by scaling the odd-order ones. This approximation neglects non-linear saturation effects in the iron and thus is only good for small corrections. The adjusted coefficients are plotted as a function of z in Fig. 192. One can see that there are significant higher order terms beyond about $z = 120$ cm, with the C_2 component dominant. Once the final tune is determined by this approximation, a full TOSCA calculation based on the tune values may be performed to verify the results.

LSA tune The LSA tune is closely related to the SSA tune. It is produced by sliding all the magnets and detectors forward by 2.32 m. The QD is operated with the same fields, so that the central ray follows the same path through the QD and the detectors. The fields in the two

Table 34: SHMS Optics Parameters for SSA and LSA Tunes. Coordinates are given as (horiz,vert) distance from nominal target center.

Parameter	***SSA tune***	***LSA tune***
Q1, Q2 mechanical length	189.0 cm	189.0 cm
Q1, Q2 magnetic length	187.9 cm	187.9 cm
Q1, Q2 pole-tip radius	25.0 cm	25.0 cm
Q1, Q2 beam-pipe inner radius	20.5 cm	20.5 cm
Length from target center to Q1 center	558.5 cm	326.5 cm
Length from target center to Q2 center	857.5 cm	625.5 cm
Q1 field gradient for 11 GeV	-7.7069 T/m	-10.7436 T/m*
Q2 field gradient for 11 GeV	8.6041 T/m	9.3790 T/m*
QD beam-pipe inner radius	30.0 cm	30.0 cm
Central ray path-length to middle of QD	1290.0 cm	1058.0 cm
Coordinates of QD center	(1288.2 cm, 20.8 cm)	(1056.2 cm, 20.8 cm)
QD rotation	9.200°	9.200°
Total bend angle	18.400°	18.400°
Layout bend radius	1079.8 cm	1079.8 cm
Coordinates of layout bend center	(1116.6 cm, 1079.8 cm)	(884.6 cm, 1079.8 cm)
Total length of central ray	1850.0 cm	1718.0 cm
Central ray coordinates at focal plane	(1824.3 cm, 177.3 cm)	(1687.2 cm, 208.8 cm)
Field at QD center for 11 GeV	3.3416 T	3.3416 T
Quad component at QD center, 11 GeV	3.3416 T/m	3.3416 T/m
Minimum spectrometer angle	5.5°	10°
Maximum spectrometer angle	25°	25°
Minimum separation from HMS	16°	25°

* Maximum achievable quad gradient of 8.6 T/m limits central momentum to 8.8 GeV

quadrupoles were re-optimized by COSY in order to produce a good focus at the focal plane, which was shifted 1 meter farther back from the QD, as measured along the central ray, to avoid tipping the focal plane to too shallow an angle. By having the quads closer to the target, the solid angle acceptance is increased, as is evident from Fig. 193, in which we track the 27 standard test rays. However, this tune requires substantially higher quadrupole fields, as listed in Table 34. The values listed, corresponding to a central momentum of 11 GeV/c, exceed the capability of these magnets. The maximum central momentum that can be reached in this mode of operation is 8.8 GeV/c, for which Q1 operates at its maximum gradient of 8.6 T/m. Note that with a central momentum of 8.8 GeV/c the SHMS still accepts full energy (11 GeV/c) particles, albeit with somewhat poorer resolution. With the quads moved forward the minimum scattering angle becomes 10°.

SHMS model in the 'physics' Monte Carlo The field maps generated by COSY have been incorporated into a model of the spectrometer so that detailed simulations can be made of the SHMS acceptance, resolution, and distributions of events at the detectors. COSY-generated transformations are used to propagate particles from the target to each of the important apertures in the spectrometer. In addition, the particle trajectories can be evaluated at each detector package

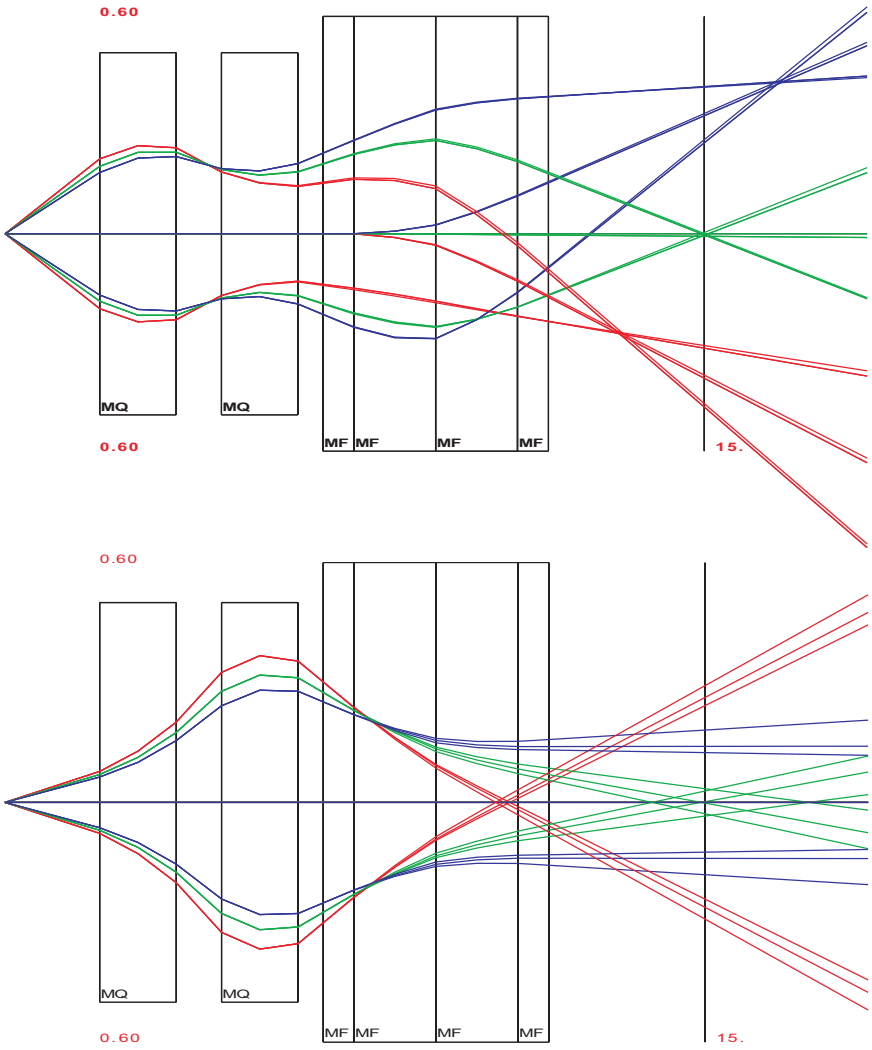

Figure 193: Rays Tracked through the SHMS by COSY for the LSA Tune. The top panel is the bend-plane projection (COSY (x, z) coordinates), while on the bottom is the transverse projection (COSY (y, z) coordinates). 27 rays are plotted for all combinations of 3 values of total momenta ($\Delta p/p_0$ = 0.1 [blue], 0 [green], -0.1 [red]), 3 values of p_x/p_0 (0.4, 0, -0.4), and 3 values of p_y/p_0 (0.15, 0, -0.15).

in order to determine the active region needed for each detector.

The SHMS model is of the same format as the existing HMS and SOS models, and so has been added to 'SIMC', the physics Monte Carlo used extensively in Hall C. This allows generation of various physics processes, taking into account the cross sections and event distributions, as well as multiple scattering and energy loss in target, spectrometer, and detector materials, and any relevant particle decays. The SHMS model includes the same level of detail as the models for the existing spectrometer, and so the simulation can be used for detailed and extremely realistic studies under a variety of conditions. In particular, it can be used to determine the acceptance and resolution as functions of target length, collimation scheme, and detector configuration.

SHMS Performance (Resolution/Acceptance)

A stand-alone Monte Carlo has been used to investigate the properties of the SHMS design as developed in the previous section. The Monte Carlo was run with the spectrometer at 90° and a target length of 70 cm. Electrons were generated uniformly over the phase space and sent through the SHMS spectrometer with the central momentum ($p_{\rm cent}$) set at 7.5 GeV/c. Events were generated over the $\delta = (p - p_{\rm cent})/p_{\rm cent}$ range of -40% to 40%, horizontal angle ($y' = dy/dz$) range of ±100 mr and vertical angle ($x' = dx/dz$) range of ±100 mr relative to the spectrometer axis. Studies were done with the large solid angle (LSA) tune (spectrometer moved forward by 2.32 m) and the small solid angle (SSA) tune.

Plots of the δ, Y_{tar}, y' and x' acceptance are shown in Fig. 194 for the large solid angle (LSA) tune (solid black line) and the small solid angle (SSA) tune (solid red line). Both tunes have a large acceptance in δ and Y_{tar}, the horizontal position. Both tunes have a flat acceptance in Y_{tar}. For the LSA tune, the δ acceptance is flat for negative δ and gradually decreases with increasing positive δ. The SSA tune has a fairly flat acceptance with a drop-off above δ = 10%. Both tunes have a sharp drop off below δ = -20%. In designing the size of the detectors, cuts of $-15 < \delta < 25$ % and $-25 < Y_{tar} < 25$ cm were used. The plots of y' and x' acceptance in Fig. 194 include these cuts. The LSA tune has about twice the x' acceptance of the SSA tune.

The beam envelope at z=0 in the detector hut is plotted in Fig. 195 for the LSA tune with cuts of $-15 < \delta < 25$ % for target lengths of 0.5, 4, 30 and 50 cm. (Note that a 30 (50) cm target viewed at 90° roughly corresponds to a ≥70 (120) cm target at ≤25°.) We use the TRANSPORT[Br80a] coordinate system in which +X is down and +Y is beam left. For the 0.5-cm target, one can see the expected hourglass shape of the X versus Y distribution and with increasing target length the waist of the hourglass expands. The bottom plots in Fig. 195 (for target lengths of 30 and 50 cm) show that the detectors have to be increased by 1.4 times in the horizontal dimension to accommodate an increase of the target length by 1.7 times . The detectors will be built for $-25 < Y_{tar} < 25$ cm, but, where appropriate, will initially only be instrumented for the 30-cm target. The beam envelope for the LSA tune is plotted in Fig. 196 at key points within the detector stack.

The effective solid angle was calculated by generating 100K events over a range of horizontal angle of $\Delta x' = \pm 0.1$, vertical angle of $\Delta y' = \pm 0.1$, $-15 < \delta < 25$ % and $-25 < \mathrm{Y}_{tar} < 25$ cm. The effective solid angle, Ω, was calculated as $\Delta x' \cdot \Delta y' \cdot \frac{\#\ \text{accepted}}{\#\ \text{thrown}}$. The LSA tune has $\Omega \approx 4.0$ msr, while the SSA tune has $\Omega \approx 2.0$ msr.

The resolutions for the target quantities δ, Y_{tar}, y' and x' for 7.5 GeV/c electrons are plotted as functions of δ in Fig. 197 for the SSA tune. For these calculations, the assumption was that the pipe which could contain the gas and mirror for the first gas Čerenkov detector will be at vacuum. This Čerenkov detector is primarily intended for experiments in which high resolutions are not needed. The solid blue curve has no multiple scattering nor wire chamber resolution in the Monte Carlo and indicates the limitations of the optics matrix used in the model of the SHMS. The blue line is nearly at zero except near the edges of the δ range, confirming that the optics matrix is adequate. The red dashed curve shows the effect of including wire chamber resolutions in the Monte Carlo. The solid black curve adds the effect of multiple scattering. For the Monte Carlo, the hydrogen target cell was a cylinder with radius 3.37 cm and a wall thickness of 0.005 inches. The combination of the scattering chamber window, air, and spectrometer entrance window was 0.6% radiation lengths. In the detector hut the material was the spectrometer's exit window (taken as Mylar/Kevlar material of 0.020 inches thickness in the simulation), air, and the material of the drift chambers. The resolutions in y' and x' are relatively independent of δ. The contribution to the resolution in y' and x' from wire chamber resolution and multiple scattering are about equal, while the Y_{tar} and δ resolutions are dominated by wire chamber resolution with multiple scattering having almost no effect at this momentum. The Y_{tar} resolution has a fairly dramatic parabolic dependence on δ. For the SSA tune, the δ resolution is seen to have a slightly asymmetric parabolic dependence on δ with a minimum at $\delta \approx$ -1%. For the LSA tune (not shown here), the δ resolution has an asymmetric parabolic dependence with a minimum at $\delta \approx$ -6%. The average resolutions for δ, Y_{tar}, y' and x' are about 0.05 %, 0.20 cm, 0.8 mr, 0.8 mr for both the SSA and LSA tunes, meeting or exceeding the requirements given in Table 31.

SHMS Detector Systems As the momentum range of a spectrometer changes, so also do the demands on the particle detector elements. At higher momenta, the degradation of angle and momentum resolution due to multiple scattering are reduced, and one can consider incorporating a low-mass detector in the upstream regions of the detector stack. The times-of-flight (TOF) of different particle species differ less, making trigger timing somewhat easier, but also making particle identification by TOF a less viable option. Particle identification using the Čerenkov effect also depends upon the relative speeds of particles, which means that Čerenkov counters must be more thoughtfully designed than at lower momenta, and that other identification techniques should be considered. Higher energy leads to larger fluctuations of the energy deposited in a total-absorption calorimeter, as there is a higher probability that some of the energy leaks out the back; this necessitates considering a thicker shower counter for the SHMS than is used in the HMS.

The above considerations lead us to a SHMS detector system design which would essentially be

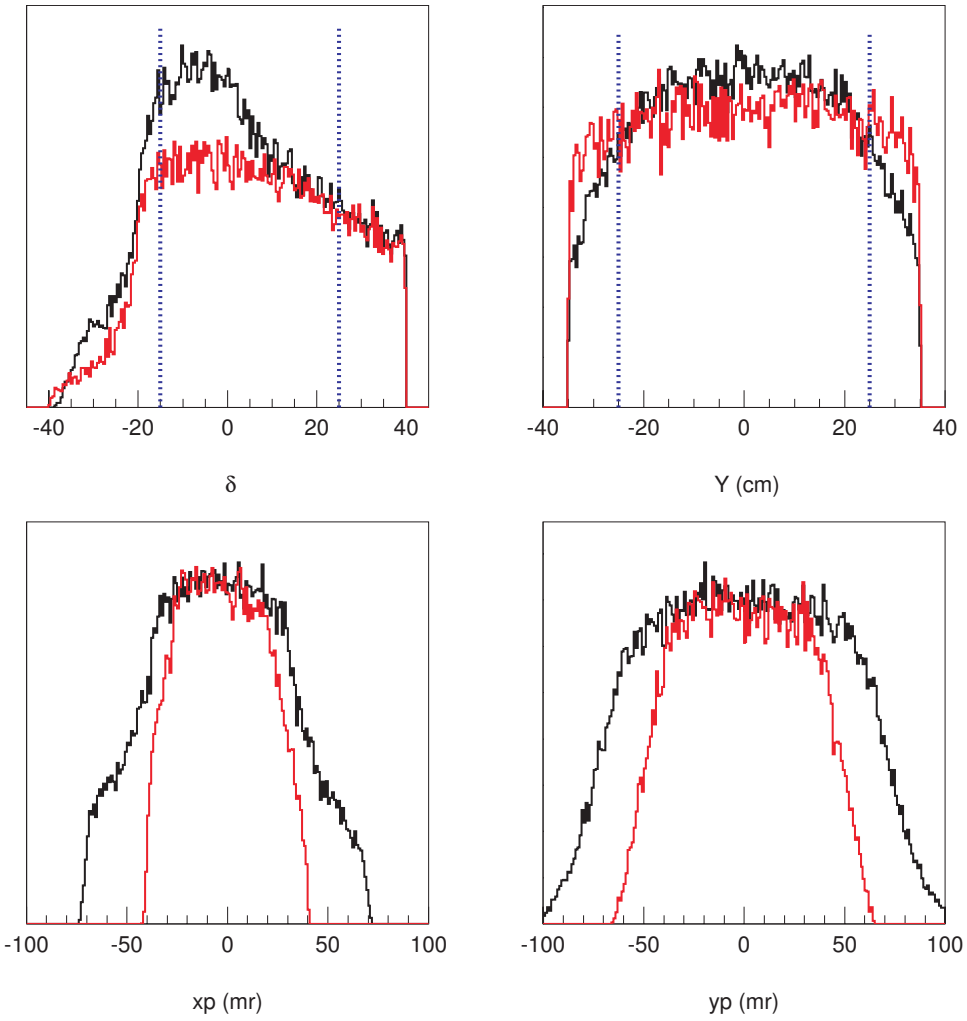

Figure 194: The Phase Space Acceptance plotted as function of δ, Y_{tar}, y' and x' for the large solid angle (LSA) tune (black solid line) and the small solid angle (SSA) tune (red solid line). The y-axis is yield in arbitrary units and the LSA and SSA yields have been scaled to match each other at the maximum. The blue dotted lines indicate the limits of $-15 < \delta < 25$ % and $-25 < Y_{tar} < 25$ cm which were used in determining the detector size. The plots of y' and x' include the cuts of $-15 < \delta < 25$ % and $-25 < Y_{tar} < 25$ cm.

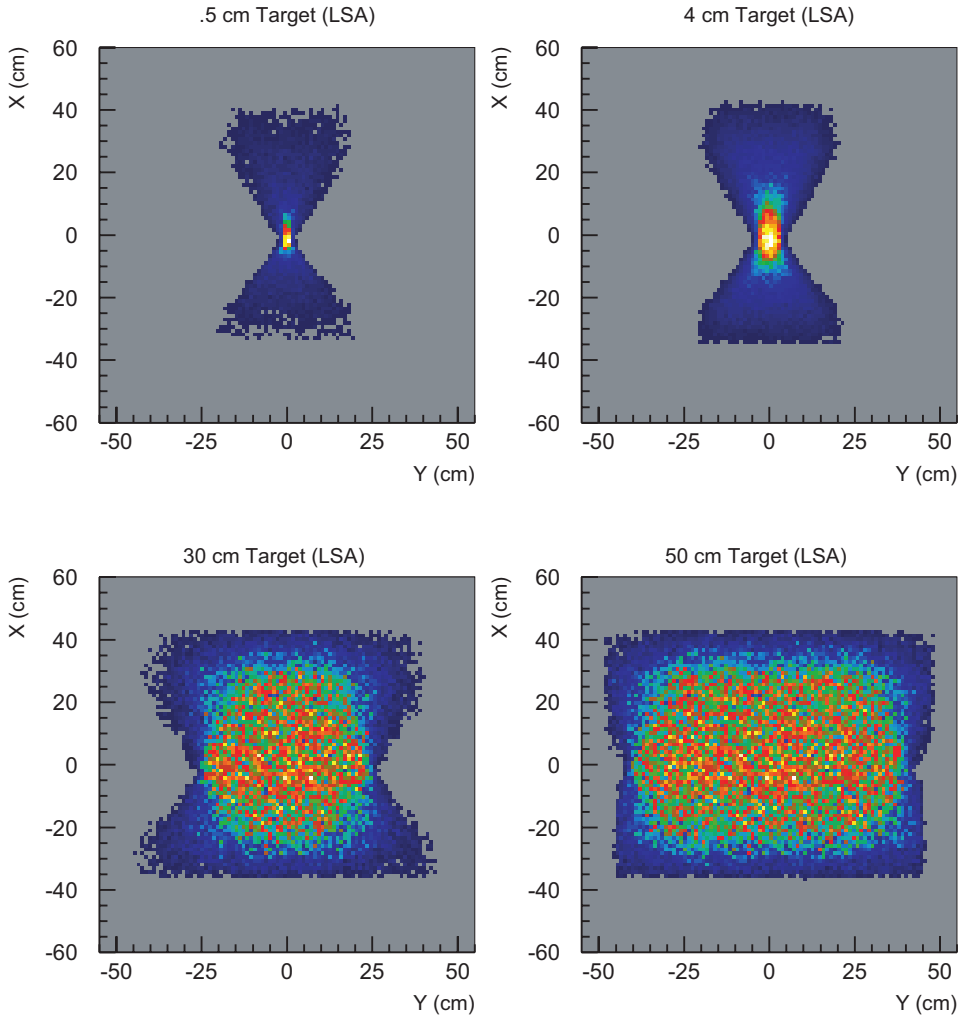

Figure 195: Plots of the Vertical (X) versus the Horizontal (Y) position at z=0 cm in the detector hut for target lengths of 0.5 cm, 4 cm, 30 cm and 50 cm. Spectrometer set for large solid angle tune with a cut of $-15 < \delta < 25$ %.

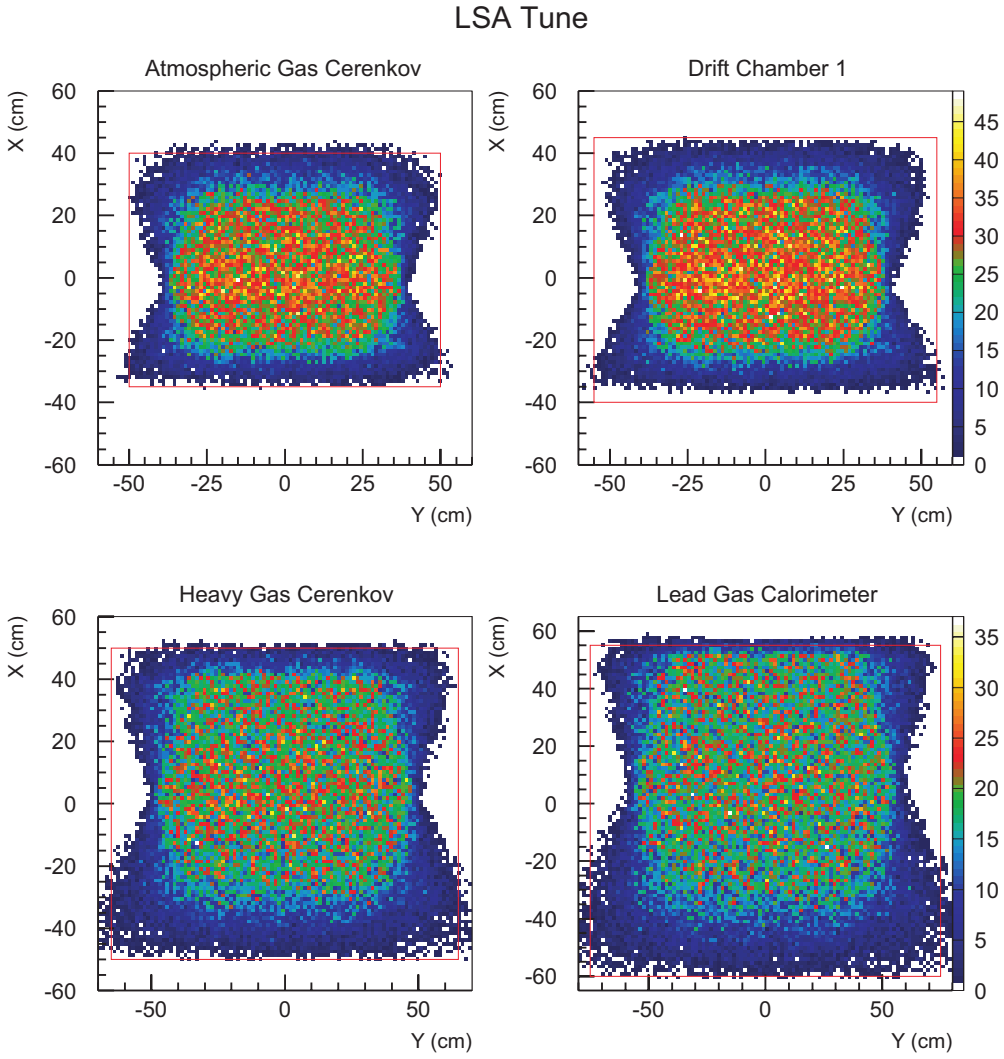

Figure 196: Plots of the vertical X versus the horizontal Y position at z=-60 cm (*Atmospheric Čerenkov*), z=-40 cm (*Drift Chamber 1*), z=160 cm (*Heavy Gas Čerenkov*) and z=320 cm (*Lead Glass Calorimeter.*) Spectrometer set for large solid angle tune with cuts of $-15 < \delta < 25$ % and $-25 < \mathrm{Y}_{tar} < 25$ cm.

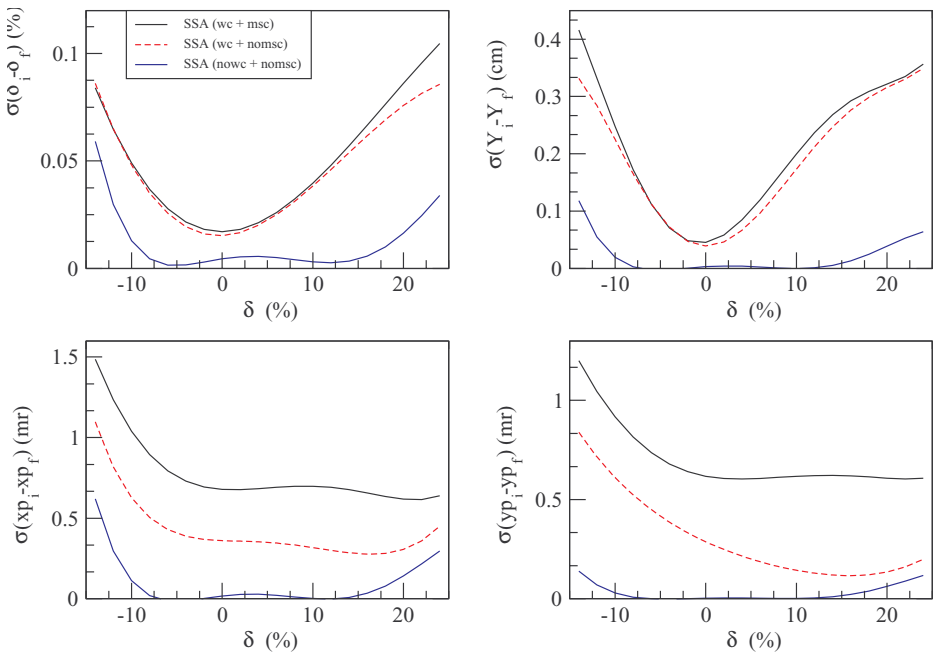

Figure 197: For the small solid angle (SSA) tune, plots of the resolutions in the target quantities δ, Y_{tar}, y' and x' as a function of δ for 7.5 GeV/c electrons. The solid black curve is the best estimate of real-world resolutions. Other curves explained in the text. The subscripts f and i refer to the reconstructed and originally generated variables.

a HMS stack modified for higher energies. However, new physics initiatives demand the inclusion of new capabilities. Measurement of the polarization of final state particles would require the inclusion of a polarimeter in the SHMS detector stack, for example. Experiments at higher rates or with low signal-to-background would benefit from improved electron/hadron discrimination, such as that provided by the addition of a transition radiation detector (TRD). Pion/kaon separation, primarily achieved by gas and aerogel Čerenkov counters, can be enhanced by recording dE/dx information in the tracking chambers and the TRD. Below, we describe an integrated system of detector components which are optimally matched to one-another and to the physics to be done in Hall C. A block diagram of the proposed detector system is shown in Fig. 198. The overall specifications for the spectrometer, developed for the physics, were summarized in Table 31.

The magnetic optics described above provides good resolution over a large acceptance. It also allows the possibility of performing experiments with a projected target length as large as 50 cm without giving up good resolution. To detect and measure this full acceptance will require that the detectors cover a large area. The required detector sensitive areas are given in Table 35. Our plan is to build the mechanical components of the detectors large enough to achieve full coverage of the 50-cm (projected) target over a 40% momentum bite (-15% $< \delta <$ +25%). However, until such time as the full acceptance is actually needed by an experiment, only the central regions of the detectors (covering a 30-cm projected target) will be instrumented.

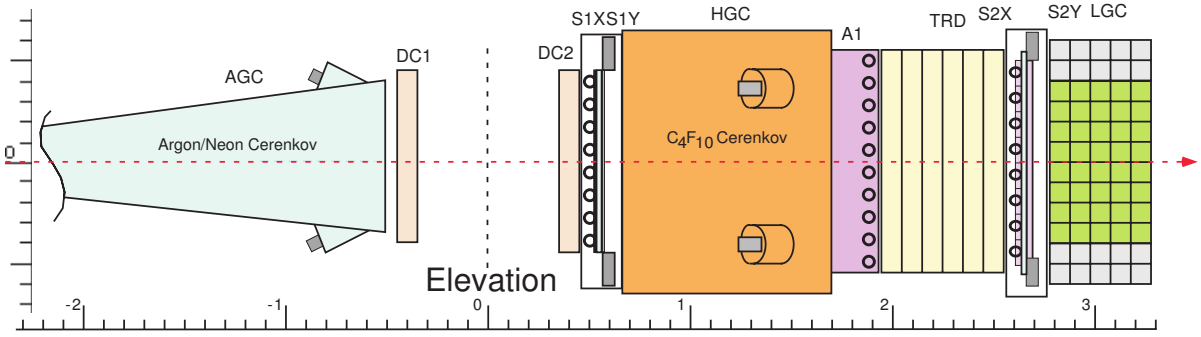

Figure 198: Block Diagram of SHMS Detector Arrangement.

Table 35: Sensitive Areas of the Detectors for Momentum Range -15% $< \delta <$ +25% , for both 30-cm long and 50-cm long targets.

	30-cm Target		50-cm Target	
Detector	X size	Y size	X size	Y size
Atm. Gas Č	75	80	75	100
Drift Chambers	85	80	85	110
Scint. Hodo 1	90	90	90	110
Heavy Gas Č	100	95	100	130
Aerogel Č	110	100	110	140
TRD	110	100	110	140
Scint. Hodo 2	110	100	110	140
Shower Counter	115	120	115	150

Wire Chambers The SHMS tracking system will provide the only measurement of particle momentum and production angle in the spectrometer. Given an adequate description of the magnetic optics, the momentum and production angles are determined by measuring enough of the track to generate a track vector at the reference plane, then projecting it back to the target.

Although Multiple Coulomb Scattering is reduced at higher momentum, it is still a significant effect limiting momentum and angular resolution, even at 11 GeV/c. We have considered several alternatives to wire chambers for tracking in the SHMS, but conclude that gas drift chambers remain the best choice to simultaneously provide the necessary position resolution while keeping the detector mass low.

The particular design we have chosen is based upon the successful SOS drift chambers, with only minor modifications suggested by the different SHMS optical parameters and lessons learned from the original design. These chambers provide better than 180-μm single-plane resolution and operate at rates of at least 1 MHz per wire, while placing only about 0.002 radiation lengths of material in the path of particles for a stack of six sense planes. The excellent performance of the SOS drift chambers is demonstrated by the distributions of track residuals shown in Fig. 199.

A simplified diagram of the chamber design is shown in Fig. 200. These chambers are constructed using the "open plane" technique, in which individual wire and cathode (foil) planes are fabricated on a work bench, then stacked up on a rigid frame to make the chamber assembly. This method of construction is relatively simple and robust, lending itself nicely to fabrication in a modest workspace.

As a baseline, we plan to use commercially available readout electronics of the same design as presently in use in the SOS, the HMS, and other wire chambers at JLab. However, we note that there is the possibility of enhancing the particle identification power of the SHMS spectrometer if we measure the energy loss distribution of particles traversing the wire chambers. To do so would require modified electronics at the chamber and the addition of analog readout for groups of wires. A study of the feasibility and usefulness of performing a maximum likelihood analysis of these Landau distributed dE/dx samples is ongoing. Figure 201 shows the results of a simulation of such a dE/dx system for identifying kaons and pions.

Quartz Čerenkov Hodoscope The existing scintillating hodoscopes in Hall C are used for a surprising number of essential functions: to provide a trigger which is approximately 100% efficient for minimum ionizing particles[7], to reject accidental coincidences in multi-arm experiments, to help measure the efficiency of the tracking system, and to provide Particle Identification (PID) by time-of-flight (TOF).

While the first three functions listed above will still be critical for the SHMS, the PID function

[7]For common detector materials, this corresponds to $\beta\gamma \simeq$ 3-4, so a "realistic worst case scenario" is the detection of protons of momenta 3-4 GeV/c.

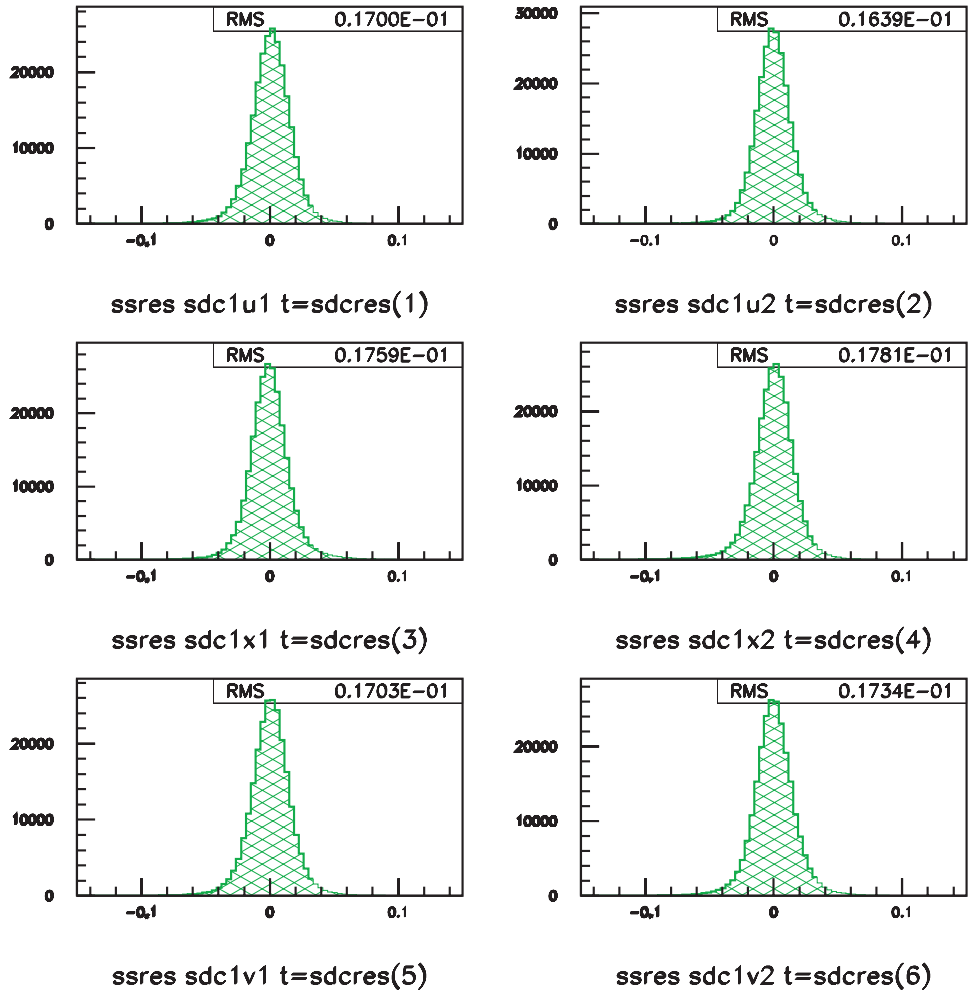

Figure 199: Measured Residual Distributions in the SOS Wire Chambers. The figures show the deviations (in centimeters) between measured hit locations in each wire chamber plane and the projected position of the associated fitted track as it passes through the wire plane. In each case track fits were performed without using the measurement from the wire plane under study. Typical residual widths are 170 microns (RMS).

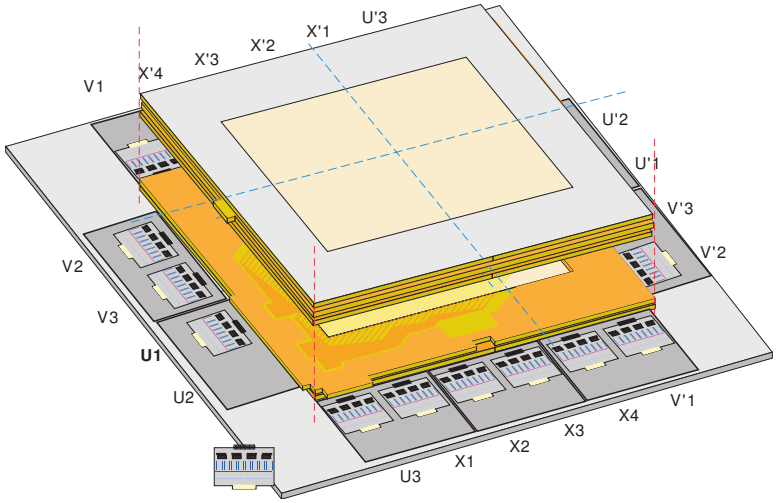

Figure 200: Block diagram of the SHMS Wire Chamber Assembly. The chamber is built by stacking individual wire and foil planes, each of which is fabricated separately using precision tooling.

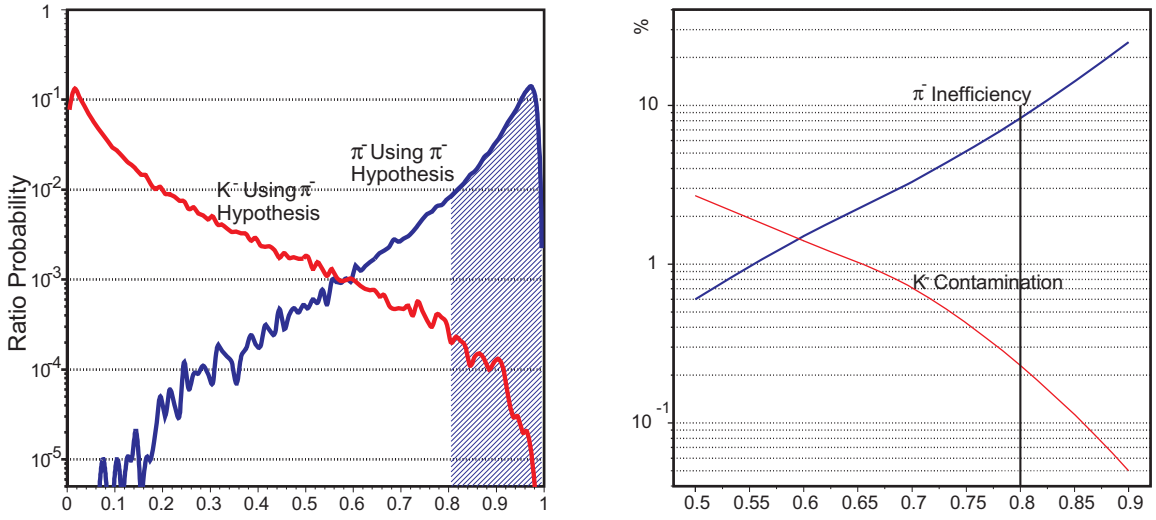

Figure 201: Pion/Kaon Discrimination using a Likelihood function applied to simulated energy loss distributions for 7 GeV/c particles in 12 wire chamber planes. For the (pion/kaon) hypothesis, only the eight (highest/lowest) measured energies are used. Left: the distribution of pion likelihood ratios $R = \frac{L_\pi}{L_\pi + L_K}$ when the incident particle is a kaon or a pion. Right: the pion inefficiency and the kaon contamination as a function of the choice of cut, when equal numbers of pions and kaons are passed through the system.

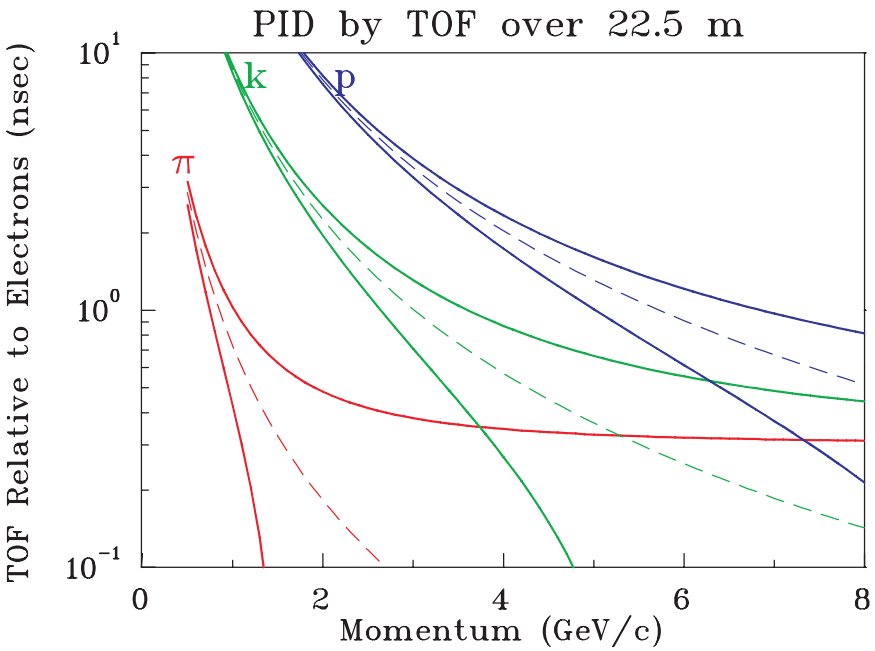

Figure 202: The dashed lines represent the time-of-flight (relative to electrons) versus momentum. The vase-shaped envelopes in solid lines demonstrate the limitations due to finite timing resolution ($\pm$ 1.5σ with σ = 200 ps assumed). At the points where the solid lines first intersect, the separation is only 3σ.

by TOF over the short $\simeq$ 2.2-m baseline inside the SHMS hut will be of little use at the higher average energies of the upgrade. Figure 202 shows that, even over a 22.5-m distance from the target to the detector stack, particle identification by TOF is of limited use. Generally speaking, efficient, high-confidence PID will require extensive use of other technologies such as Čerenkov detectors, and that the time resolution requirement for the hodoscope system may therefore be relaxed. This means that the front hodoscope array can be made thinner (5mm versus the present 10mm in the HMS and SOS) which will help reduce the production of knock-on electrons which would otherwise deteriorate the performance of downstream Čerenkov detectors. Meanwhile, the rear hodoscope array can be made quite thick (10mm-25.4mm) since it will be the last element before the electromagnetic calorimeter.

Taking into account the essential functions, and folding in our experience with the Hall C scintillating hodoscopes, we arrive at the following specifications for the SHMS hodoscopes:

- Trigger: Because it is the heart of the SHMS trigger, the hodoscope must have $\geq$ 99.9% trigger efficiency for minimum ionizing particles. To help ensure high efficiency, the pulse

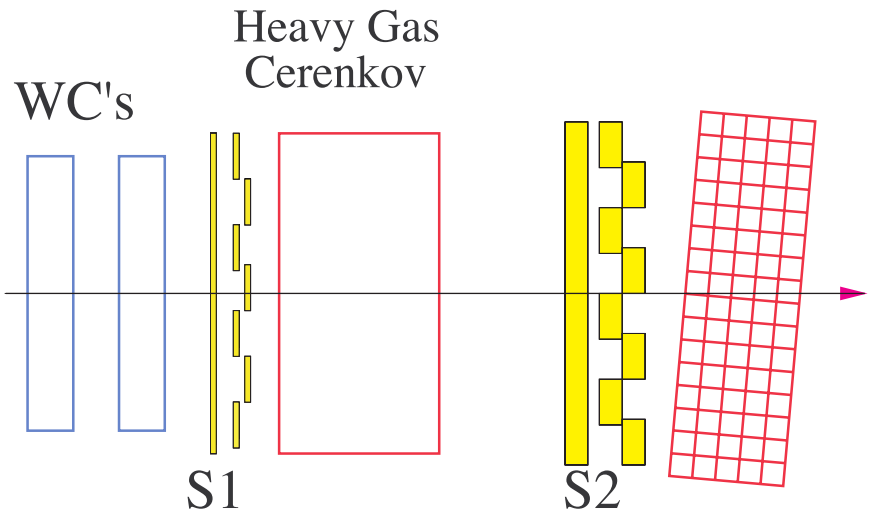

Figure 203: The thin S1 X and Y arrays will be located immediately after the wire chambers. The thicker S2 arrays will be located just before the electromagnetic calorimeter. (Drawing not to scale.)

height variation across an element should be less than 10%. There must also be sufficient redundancy such that an $S_1 \cdot S_2$ coincidence is robust with respect to the inefficiency (or even loss) of a few channels. The detector should also be insensitive to background.

- Rejection of Accidentals: The mean-time resolution of the SHMS focal plane must be at least 100 ps (rms). This will easily permit a coincidence time resolution of 200 ps (rms) so that a $\pm$1-ns cut (single beam bucket) on coincidence time would remove only the tails of the good event distribution beyond 5σ.

- Wire Chamber Tracking Efficiency: The segmentation of the hodoscope X and Y elements has to be sufficiently fine to define a beam of particles which pass through the active region of the wire chambers.

- The hodoscope should have minimal adverse impact on downstream detectors.

- The hodoscope should have a 10-year lifetime before major overhaul.

The solution which meets all of the above specifications is two pairs of X-Y hodoscopes (Fig. 203), named S_1 and S_2, similar to those currently installed in the HMS and SOS. The two arrays would be separated by roughly 2 m, with S1 following the Wire Chambers and S2 just before the Calorimeter. The new features which we would like to emphasize are that

i. S1 will be made of "thin" (*e.g.* 5mm), scintillator elements with long attenuation length BC408,

ii. S2 will consist of a relatively "thick" (*e.g.* 2cm-3cm) quartz Čerenkov radiator elements, and

Table 36: Nominal dimensions for the hodoscope elements of each of the four arrays. There are eight elements per plane.

Element	Material	Width	Length
S1X	5 mm BC408	11.3 cm	110 cm
S1Y	5 mm BC408	14 cm	90 cm
S2X	2.5 cm Quartz[9]	14 cm	140 cm
S2Y	2.5 cm Quartz	18 cm	110 cm

iii. standard 12-stage PMTs like the XP2262B will be employed, operated at low anode currents for extended lifetime.

Since the existing Hall C hodoscopes are made of scintillator, the most dramatic change listed above would be the use of a quartz Čerenkov for the S2 arrays. Simulations by Simicevic[Si01] for the $Q_{weak}(proton)$ experiment indicate that it is reasonable to expect several hundred photoelectrons (p.e.) for a 1-meter length quartz radiator with a moderately good surface reflectivity. A quartz Čerenkov detector operated at a threshold of 100 p.e. could be essentially 100% efficient and blind to low-energy backgrounds, resulting in a much cleaner $S_1 \cdot S_2$ trigger. This capability is critical for the clean detection (and accurate tracking efficiency determination) of protons in extremely low cross section measurements[8] at a CW facility.

Each of the four arrays will have eight rectangular bars of scintillator or Čerenkov radiator. The active area of the arrays is designed to have $\simeq 100\%$ acceptance of the beam envelope for the full momentum bite and target acceptance of the large solid angle tune. The SHMS beam envelope simulations can be found in Section 3.C.3. A summary of the nominal hodoscope dimensions is given in Table 36. Finally, with one PMT on each end of a scintillator or Čerenkov radiator paddle, the total number of SHMS hodoscope channels will be 64.

Particle Identification

Overview Hadron identification for momenta up to 11 GeV/c will be fundamentally different from that of the HMS-SOS detector systems. With increasing momentum it becomes more and more difficult to distinguish hadrons by time-of-flight measurements. With the 2.2-m flight path in the detector hut, kaon-pion separation by time-of-flight becomes infeasible at roughly 2 GeV/c. At 3.5 GeV/c also proton-kaon separation will no longer work. Coincidence timing with a hadron flight path in the SHMS of 22.5 m and a reconstructed coincidence time resolution of roughly 200 ps extends this to 4 GeV and 7 GeV, respectively. Note however, that particle identification by means of coincidence timing will in general not distinguish particles from accidental coincidences and therefore will lead to an irreducible background that must be subtracted. Therefore, at high

[8] *e.g.*, $d(\gamma,p)n$ at high s and $A(e,e'p)A-1$ at high Q^2.

momenta one must rely on other means of particle identification, *e.g.* Čerenkov detectors, dE/dx measurements, and Transition Radiation Detectors (TRD).

As described in detail below, the Super-High Momentum-Spectrometer will draw upon a variety of techniques to achieve particle identification over its entire momentum range. A global outline of the scheme is shown graphically in Fig. 204, where the discrimination power is shown as the significance of the measurements (number of standard deviations) in the various PID detectors versus the particle momentum.

Electron identification can always be accomplished by use of energy measurements in the electromagnetic calorimeter, and optionally improved upon with a TRD. Over the SHMS momentum range, electrons will always radiate in Čerenkov counters, so these devices will also contribute to electron tagging. For extreme cases at high momentum and low signal to background, such as measurements at $x > 1$, we envision adding another Čerenkov counter in place of the last section of vacuum pipe just upstream of the first wire chamber. This device, using a Ne-Ar mixture at atmospheric pressure, can have its index of refraction tuned to enhance either electron-pion or pion-kaon discrimination at high momentum.

For hadron identification the following PID strategy can be employed:

~ 1 to ~ 3 GeV/c: Kaon-pion separation can be achieved with the appropriate choice of one aerogel Čerenkov. A time of flight path of 2.2 m with a TOF resolution of 200 ps still allows one to distinguish protons from kaons at the 3σ level up to 2 GeV/c. At the high end of this range, proton PID can be improved with the use of an additional aerogel counter with n=1.02.

$\sim$3 to $\sim$5.5 GeV/c: Pions will trigger a C_4F_{10} gas Čerenkov. The C_4F_{10} pressure will be adjusted such that kaons do not radiate. Kaons will trigger an $n = 1.015$ aerogel Čerenkov.

$\sim$5.5 to 11 GeV/c: Pions will still trigger the C_4F_{10} gas Čerenkov. An atmospheric pressure gas Čerenkov counter will be inserted upstream of the first wire chamber and filled with an Ar-Ne mixture to provide a pion tag or an additional electron tag. At these higher momenta the multiple scattering in this added detector will be tolerable.

Thus, an appropriate choice of combinations of detectors and techniques will allow the SHMS to provide useful particle identification over its entire momentum range. The remainder of this section will describe each of these detectors.

Shower Counter The SHMS magnetic spectrometer is aimed to cover small forward angles and higher momentum settings not available so far in Hall C[WP01]. When identifying electrons at these settings, good particle identification is needed to suppress high hadron background. Lead glass electromagnetic calorimeters are well suited to this purpose.

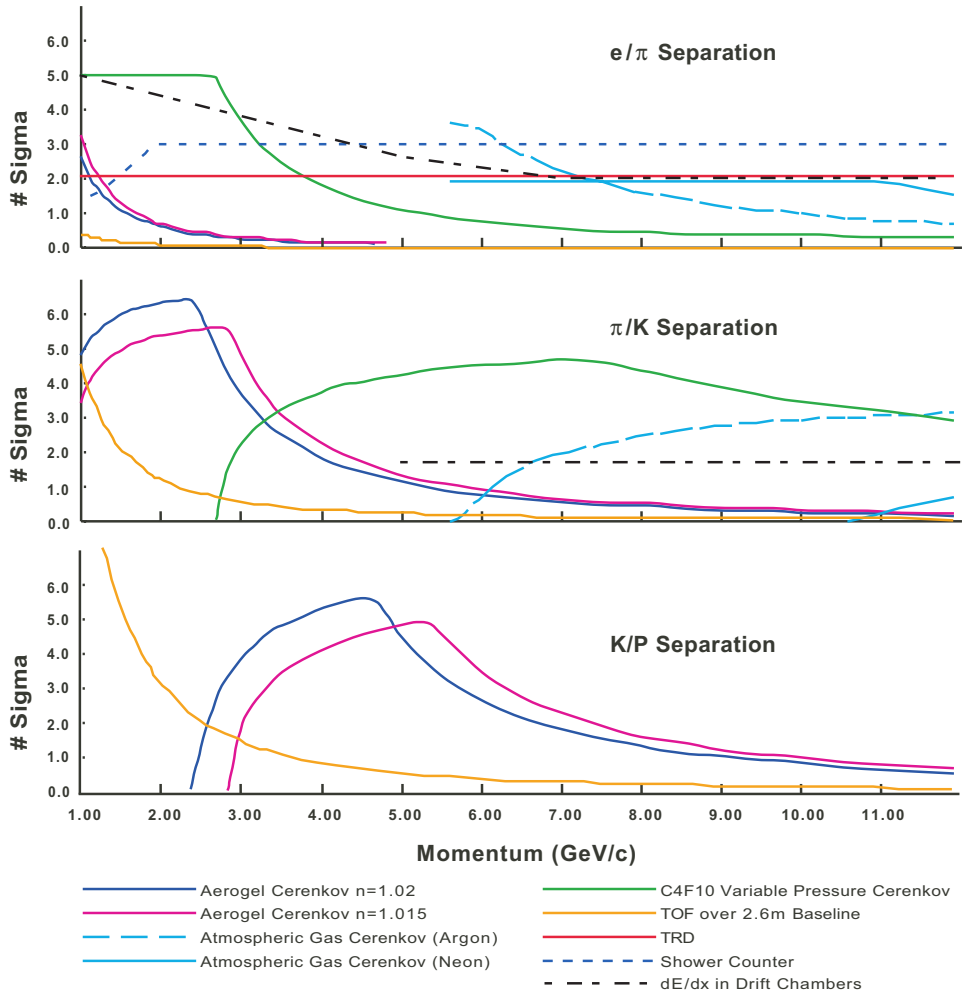

Figure 204: Particle Identification Resolving Power over the SHMS Momentum Range. The vertical scale in each graph is number of standard deviations which separate the two particle types shown, calculated for all of the relevant detectors in the system.

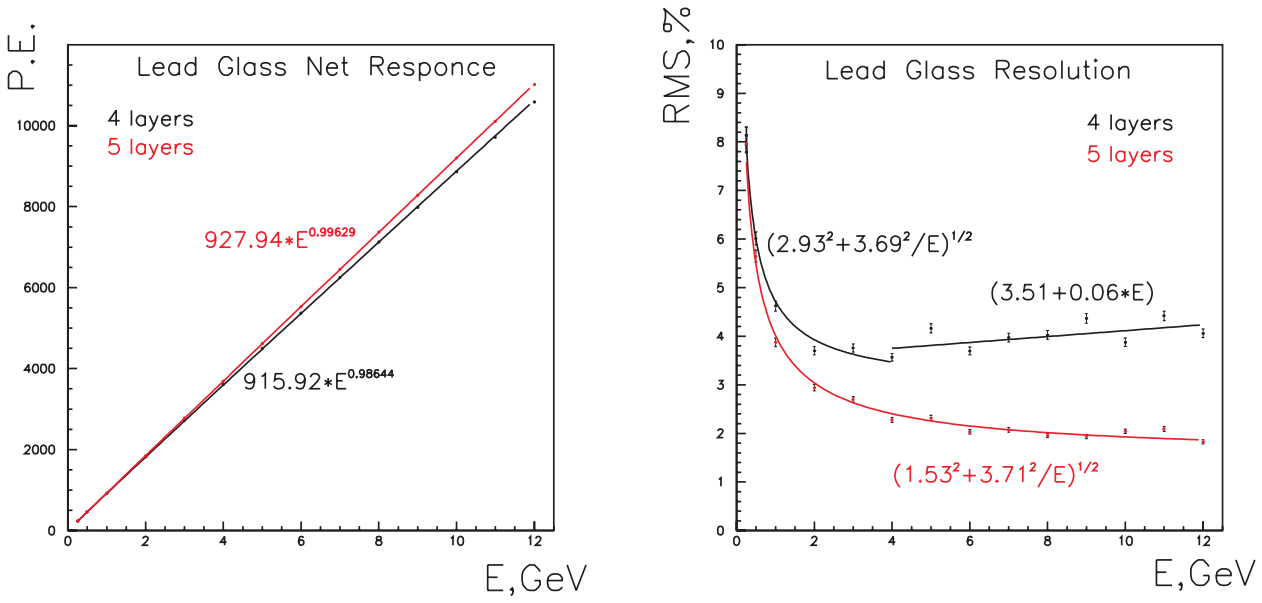

Figure 205: EGS4 Monte Carlo simulation of the linearity (left panel) and resolution (right panel) of a TF-1 Lead Glass modular calorimeter. The calibration, coordinate correction and electronic effects are not included.

The design of the SHMS electromagnetic calorimeter is similar to the existing HMS and SOS calorimeters in many respects. The HMS calorimeter consists of $10 \times 10 \times 70$ cm^3 TF-1 Lead Glass rectangular blocks wrapped in thin aluminized mylar and in tedlar film for optical tightness. The characteristics of the TF-1 lead glass are: density $\rho = 3.86$ g/cm^3, refractive index n=1.65, radiation length $R_L = 2.74$ cm. The blocks are arranged in four layers for a total thickness of 40 cm (14.6 radiation lengths). Photomultiplier tubes (Philips XP34462B) are mounted at both ends of each block in the first two layers and at one end for the remaining layers. The modules are equipped with ST–type fiber adapters for the gain monitoring system.

Figure 205 shows the results of a Monte Carlo simulation for the lead glass calorimeter. As can be seen from the left panel, the calorimeter is linear within 3.5% up to electron energies of 12 GeV. The energy resolution of the HMS calorimeter (PMTs mounted on one end of each block) measured in the energy range 0.5–4.0 GeV is given by

$$\frac{\Delta E}{E}(\%) = \frac{6.1}{\sqrt{E(GeV)}} + 0.3 \tag{77}$$

and is comparable to the resolution of similar devices[PDB]. The SOS calorimeter is somewhat better in this respect[Ar98]. More details on the HMS and SOS calorimeter construction and performance can be found in Ref. [Ar98]. The performance of the calorimeters has not deteriorated significantly in the 7 years since they were first installed.

The observed π^-/e^- rejection factor of the HMS calorimeter is better than $(1-5) \times 10^{-2}$ in the momentum range 0.5 to 2.0 GeV/c, with electron detection efficiency $\geq 99\%$. At these low momenta, pion rejection can be improved at the cost of electron efficiency by using a tighter cut

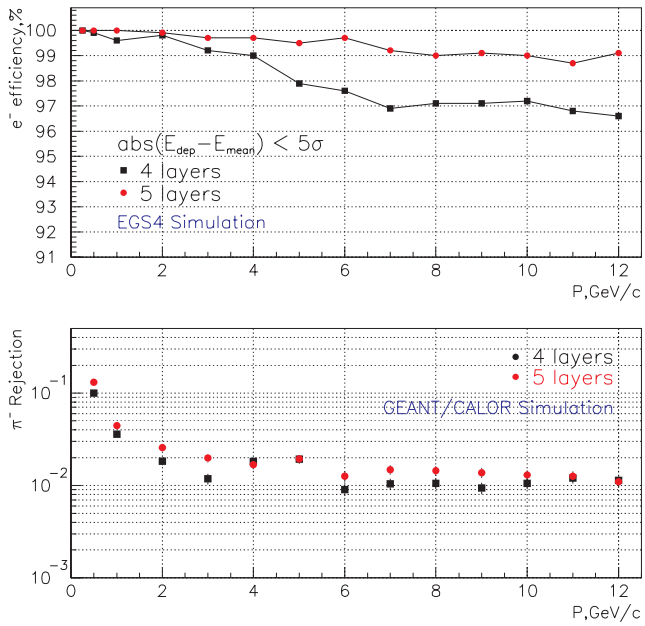

Figure 206: Electron detection efficiency (top panel) and pion rejection (bottom panel) obtained from the Monte Carlo simulation of the TF-1 Lead Glass Calorimeter. The calibration, coordinate correction and electronic effects are not included.

on the calorimeter energy. At higher momenta, the pion rejection is not significantly improved by a tighter cut.

The energy dependence of the resolution of the calorimeters indicates almost complete absorption of electromagnetic showers up to energies of ~ 4 GeV. However, at higher energies the Monte Carlo simulation predicts a slow rise of the resolution, which is a clear indication of leakage (see Fig. 205, right panel). Adding an additional layer restores full absorption, hence improving both the resolution and linearity. Adding a fifth layer also improves the electron detection efficiency (see Fig. 206, top panel), but it does not change the pion rejection (Fig. 206, bottom panel). Exploiting the transverse and longitudinal spread of the deposited energy will improve pion rejection, and the contribution of a fifth layer may be valuable in this case.

Two side by side stacks of 12 blocks are needed to cover the whole acceptance of the spectrometer (see Fig. 196) and thus 120 modules would be required. As adjacent blocks will be optically decoupled, the light will be collected with PMTs on both ends of the calorimeter blocks. The calorimeter will be deflected by small amounts in both vertical and horizontal directions to avoid cracks in between the modules.

Alternatively one can construct a lower cost, 4–layer calorimeter using only 96 modules. It will still contain most of the electromagnetic shower and hence have hadron/electron rejection capability. The leakage of energy will not significantly affect the hadron rejection, but will hurt the electron efficiency (or the electron rejection when measuring pions).

Another low-cost alternative is an assembly of 132 short modules oriented along the beam direction. A preshower wall of 24 long modules before this assembly may be helpful for the separation of minimum ionizing hadrons from just developed electromagnetic showers. The deepness of the calorimeter should be optimized to get good rejection across the SHMS momentum range.

Atmospheric Pressure Čerenkov One of the typical uses of the SHMS will be to detect highly inelastic scattered electrons. At such kinematics the pion background can be significant, so a reliable method of electron identification is required. Threshold Čerenkov detectors are excellent tools to use when the particle velocity β is greater than phase velocity of light in the medium c/n. The minimum momentum at which a particle will exceed the phase velocity of light in the medium is given by:

$$P_{min} \cdot c = \frac{M \cdot c^2}{\sqrt{n^2 - 1}} \tag{78}$$

Thus, if we require 10 GeV/c pion to be under threshold, then $n - 1$ must be 0.0001 or smaller, which can be achieved either by choosing low-pressure gases, or certain noble gases at STP. For example $n - 1 = 0.000067$ for Ne, $n - 1 = 0.000033$ for He.

The main characteristic of threshold Čerenkov detectors is the number of detected photons. For very low refractive-index gases the number of emitted photons is extremely small. At $p > 9.0$ GeV/c a gas Čerenkov for electron-pion discrimination should be over 2.5-3 m long in order to have an adequate number of photoelectrons. A β=1 particle traversing a 3 m long Ne radiator will produce about 30 photons in the visible light range (300-700nm). Most PMTs are not very sensitive below 300 nm. Since the production has a λ^{-2} dependence, and $n(\lambda)$ goes to unity at short wavelengths, the Čerenkov light produced will be peaked in the ultraviolet (100-300nm). Using these photons will double the number of photoelectrons from the photocathode [Ar98, So99]. PMT windows coated with p-terphenyl, which absorbs UV light and retransmits it in the range of 390 nm, increase the PMT response by about 90% compared to the uncoated tubes[So99]. The expected number of photoelectrons will be $\simeq 10 - 12$.

The solution to adjust the refractive index by using the noble gases at STP appears more attractive than the use of a low-pressure tank. The low-pressure approach requires a 3 m long vacuum sealed volume. Having this volume under-pressurized tends to gradually take in O_2 and H_2O which can change not only the threshold condition, but also absorb the ultraviolet part of the Čerenkov radiation. Further, using Ne and Ar at STP allows the windows of the Čerenkov tank to be made very thin (possibly from tedlar). This will aid in minimizing multiple scattering in front of the drift chambers.

The atmospheric Čerenkov tank we propose would replace the final 3 m of the vacuum pipe as it enters the SHMS detector hut. The diameter needs to be only about 60 cm at the upstream end, and cover 75×100 cm^2 at the downstream end. A vacuum window with the same scattering properties as the standard one would be installed upstream of the Čerenkov counter. The Čerenkov windows and mirrors and their supports will be made lightweight so as to keep multiple scattering

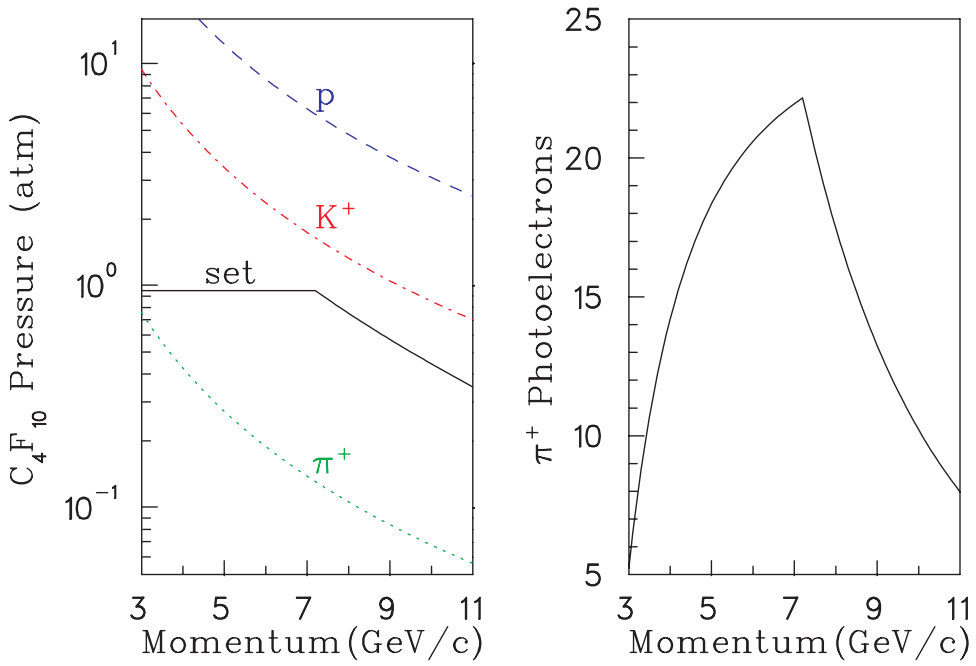

Figure 207: (Left) Threshold C_4F_{10} pressure required for Čerenkov light generation from the particles indicated. The solid curve indicates the operating pressure planned for the detector. (Right): Number of photoelectrons anticipated for the detector, taking into account the transmittance, reflectivity, and quantum efficiency functions of the detector components.

at a minimum. Even then, the detector would only be compatible at the high end of the SHMS momentum range.

Heavy Gas Čerenkov Above ~ 3 GeV/c, hadron species cannot be reliably distinguished by time of flight over the 2.2-m baseline planned for the SHMS detector stack, and so information from Čerenkov detectors becomes increasingly relevant. An aerogel Čerenkov detector with $n = 1.02$ will provide $\pi^{\pm}/K^{\pm}$ discrimination only up to 2.4 GeV/c. Beyond this momentum, a gaseous Čerenkov detector is required. Based on the excellent operational experience at JLab and elsewhere, we propose to construct a threshold Čerenkov using the heavy perfluorocarbon (PFC) gas C_4F_{10} as a radiator. This gas has an index of refraction of 1.00143 at standard temperature and pressure, and so can be used here over a wide range of incident particle momenta.

The solid curve in the left panel of Fig. 207 indicates the gas pressure we propose to use at each SHMS central momentum setting. It is expected that the detector gas pressure will be remotely controlled from the counting room as the spectrometer momentum is changed. We assume 0.95 atm. pressure from 3.4 GeV/c to 7.0 GeV/c, and sub-atmospheric pressure at higher momenta. The gap between the 'set' and 'K^+' curves above 7 GeV/c takes into account the +25%/-15% momentum bite of the SHMS, and a possible 0.1-atm error in the setting of the gas pressure regulator. We do not anticipate the detector being used for π^+/K^+ separation at momenta below 3.4 GeV/c.

Figure 208 shows a schematic design for the heavy gas Čerenkov. The enclosure is a cylinder

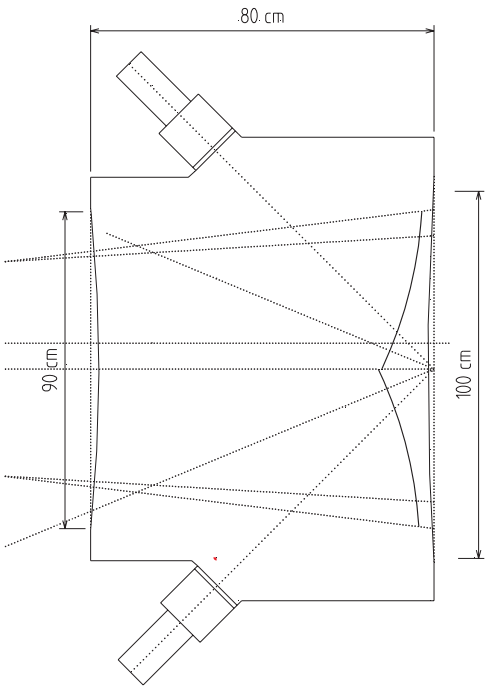

Figure 208: Schematic Design for the SHMS Heavy Gas Čerenkov Detector.

of nonmagnetic stainless steel, with the PMTs located outside, viewing through a 1-cm thick UV-grade fused silica window. This allows for better isolation of the pressurized cavity, and allows one to maintain proper PMT-mirror optical alignment should the PMT require servicing. Four mirrors and photomultipliers are required to cover the SHMS beam envelope; they should be of the highest possible quality. As a reference design, we have selected the Photonis[PHOT] XP4508B 5" photomultiplier tube. This is similar to the PMT currently used in Hall B, except that it has a flat face of fused silica, which allows for flush mating with the quartz window. A custom-design voltage divider with boosted voltage between the photocathode and the first dynode will be used to provide optimum focusing of the photoelectrons, and so minimize losses within the dynode chain. To minimize abberations, the mirrors should be thin glass, which can be structurally reinforced outside of the beam envelope. Protected aluminum mirror coatings with $> 90\%$ reflectivity down to 200 nm are commercially available[LAM10]. We propose to use $0.020''$ titanium for the particle entrance and exit windows, which is the same material used on the G0 spectrometer [Be02c].

C_4F_{10} is very expensive, and so a recovery system is required. C_4F_{10} has excellent UV transmission characteristics (97%@170 nm) provided it is kept pure. A filter and cold trap may be desirable additions to the gas recovery system, to maintain the required gas purity. Both oxygen and water absorb strongly below 200 nm, and should be kept below 0.1%. Residual nitrogen has an effect on the refractive index, and should be kept constant and below $< 1\%$.

The right panel of Fig. 207 indicates the number of detected photoelectrons expected from a π^+ for a 70-cm radiator length. The C_4F_{10} transmission, mirror reflectivity, quartz transmittance,

and PMT spectral characteristics, as well as possible optical misalignment, were all taken into account. The resulting π^+ detection inefficiency, assuming that an off-line cut is placed at < 1.5 photoelectrons to eliminate knock-on events, is less than 0.1% for all momenta between 3.4 and 10.3 GeV/c, and rises to a modest 0.3% at 11.0 GeV/c.

In conclusion, a heavy gas Čerenkov detector, utilizing a C_4F_{10} radiator with variable pressure between 0.4 and 0.95 atm., appears to be a practical way to obtain reliable π^+/K^+ separation within the SHMS.

Transition Radiation Detector The purpose of the transition radiation detector (TRD) is to separate electrons from pions. This is possible because ultra relativistic charged particles emit *transition radiation* (TR) in the form of x-rays when they traverse a dielectric boundary[Gi46]. TRDs are composed of multiple modules stacked together where a single module contains a radiator and x-ray detector (*i.e.* multiwire proportional chamber). Each radiator is made up of many dielectric interfaces of low-Z material to increase the TR yield. TRDs typically have a threshold of $\gamma = 1000$, hence only electrons will produce TR photons in the momentum range of the SHMS. In general, particle identification is accomplished either by examining the total energy deposited in the detector or by cutting on the number of high energy clusters (typically above 5–7 keV) deposited along the track. It has been shown that there is improvement in the particle separation if cluster counting is performed[Lu81a, Fa81]. This is because the number of clusters obeys a Poisson distribution while the total energy has a long Landau distributed tail. The pion rejection factor (PRF), which is inversely related to the pion efficiency, is largely dependent upon the length of the detector, as shown in Fig. 209 with smaller effects coming from the type of radiator, chamber, electronics and particle identification method[PDB].

The detector will be located between the heavy gas Čerenkov and the back hodoscope planes and will be about 60 cm long. To maximize the PRF, uniformly spaced foils of polyethylene would be close to ideal (lithium foils being ideal), but due to the relatively large active area of the detector (110×140 cm^2), carbon fibers or polyethylene foam will be considered. Using a fiber or foam radiator decreases the PRF by a factor of about 2 when compared to foils. The radiator will be 50 mm thick with a mean foil thickness of about 17 μm and a mean gap or pore size of about 200 μm. This corresponds on average to 230 foils per radiator which will produce about one detected TR x-ray per module. The x-ray detector will be a xenon filled longitudinal drift proportional chamber to facilitate cluster counting. Since xenon gas is expensive, the chamber gas will be recirculated and filtered. Figure 210 shows a sketch of a single TRD module and the pulse distribution. The longitudinal drift will be 20 mm and, if a 90% Xe/10% CO_2 gas mixture is used (drift velocity $\sim$ 25 mm/μs for $\mathcal{E} = 3$ kV/cm), the maximum drift times will be about 0.80 μs. The proportional region will be 8×5 mm^2 (anode wires spaced by 5 mm). Monte Carlo simulations which include hadronic showers and δ-ray production will be needed to determine if this segmentation is sufficient. Special attention must be paid to the exit cathode plane to reduce bulging due to pressure changes and the "hydrostatic" pressure inside the chamber. The electronics

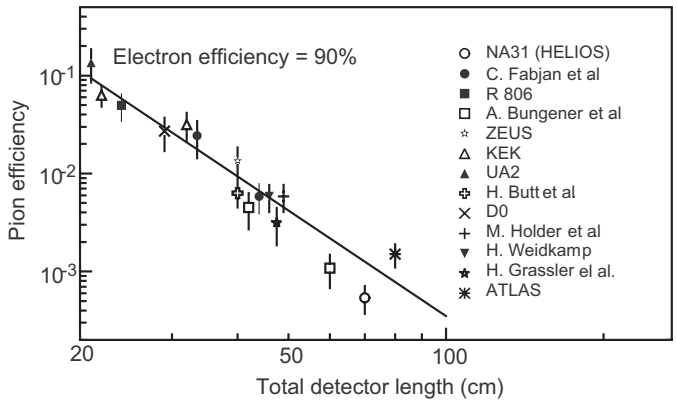

Figure 209: Pion Efficiency Measured (or Predicted) for different TRDs as a function of the detector length for an electron efficiency of 90%. (Figure from Ref. [PDB])

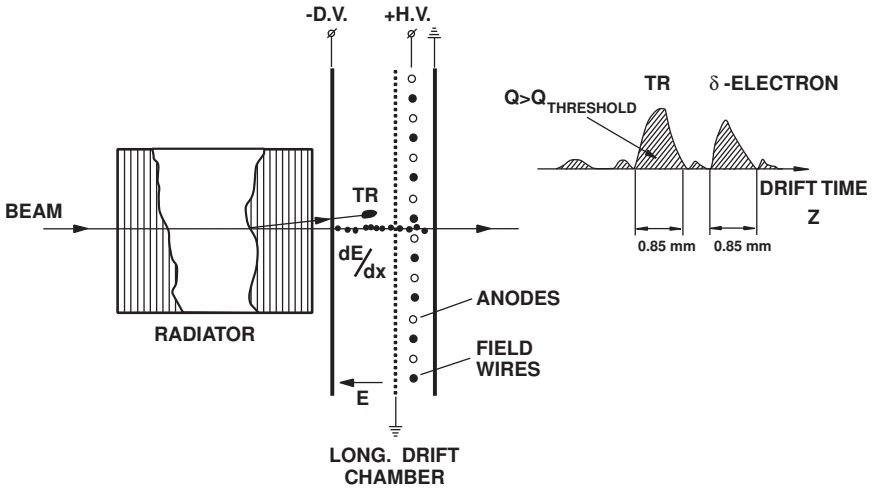

Figure 210: Single module with time expansion chamber (TEC) which includes a drift region and a proportional region. The output signals will consist of uniform dE/dx ionization with localized TR clusters and δ-ray clusters.

on each anode wire will consist of a preamplifier, a shaping amplifier and an 8-bit flash ADC.

At least six modules will be used for the TRD with a total length of about 60 cm. At 90% electron efficiency, this will result in a PRF of about 200 - 300. At 95% electron efficiency, the PRF will reduce by a factor of 3 or 4, but if a higher rejection factor is needed, additional modules could be used and/or a foil radiator could be used. Off-line analysis which includes more sophisticated statistical methods (*i.e.* likelihood) and an intelligent cluster threshold will also improve the PRF. This intelligent threshold will vary the threshold with drift time, thus taking advantage of the energy dependence of the photon's range in the chamber. Since the TR yield tends to saturate at $\gamma \sim 8000$, the PRF will be flat over the SHMS momentum range. The combination of the TRD, shower counter and a Čerenkov will be more than adequate to suppress any hadronic background encountered in the SHMS. Additionally, having three particle identification detectors will provide a better mechanism for systematic studies of the detector efficiencies.

Aerogel Čerenkov Counter The aerogel detectors will be standard diffusion box type detectors consisting of a layer of silica aerogel in a diffuse reflective box, read out at the sides by large 5-inch PMTs. For the SHMS, a detector with a minimum active area of 110×140 cm^2 is needed for full coverage of the beam envelope at the anticipated detector location, 2.3 m downstream from the focal plane (see Fig. 196 and Ref. [WP01]). Thus, a detector could be 110 cm in x (bending or vertical) with 5 PMTs on each side and 140 cm in y (horizontal). Allowing for an up to 10 cm thick aerogel layer the entire box will be roughly 30 cm deep (in z direction).

The technology of aerogel detectors with a diffusion box and PMTs as light collectors is well established at Jefferson Lab. The Hall C detector with $n = 1.034$ yielded 19.3 photoelectrons for $\beta = 1$ particles [Mo99a]. The two Hall A detectors, A1 with $n = 1.015$ (9 cm) and A2 with $n = 1.055$ (5 cm), yielded 8 and 30 photoelectrons, respectively [Zh01a]. The significantly better performance of A2 is certainly due in part to the higher index of refraction. Additionally, it is believed to benefit from a higher photoelectron yield of the Photonis tubes used in this detector as opposed to the Burle tubes used in the A1.

Two more detectors are currently under design, one for the HMS and another for the hypernuclear spectrometer (HKS). The HKS detector explores the possibility of segmenting the detector along the focal plane and thus increasing the rate capability. This should also be considered for the SHMS detector, *i.e.* to ensure reliable performance at the very forward angle settings possible with this spectrometer. The design with 5 PMTs on each side would allow for 5 optically separated segments. Limiting individual segment rates to 1 MHz would result in a total rate capability of 5 MHz for particles above the Čerenkov threshold. To compensate for the dead areas introduced by segmentation, a second plane with the segments offset by half a segment width would be required.

As aerogel the materials SP15, SP30 and SP50 from Matsushita Electric Works is recommended. Matsushita's aerogel has a waterproof coating that makes it hydrophobic. This removes the need for baking (in fact baking will destroy the coating) and also increases transparency. A

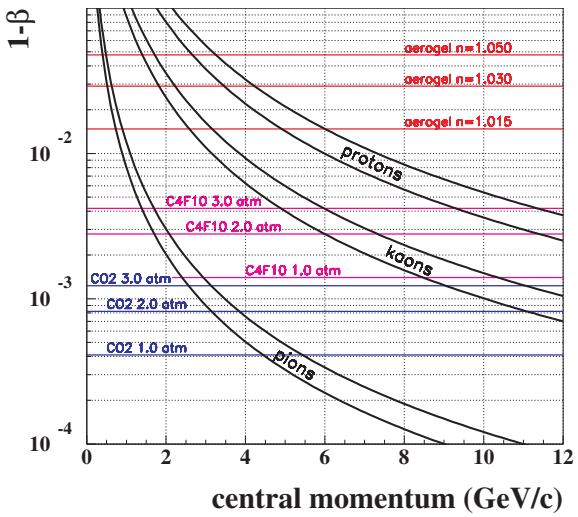

Figure 211: Hadron Velocity $1 - \beta$ as a Function of Momentum. For each particle a band is shown corresponding to a momentum acceptance of $\pm 10\%$. The horizontal lines show thresholds for different Čerenkov radiators.

low-cost 5-inch PMT (Photonis XP4572) has been successfully employed in the Hall A A2 detector and should also be considered for the detector proposed here. Figure 211 shows the thresholds for these materials as a function of momentum.

The performance of the detector has been simulated with D. Higinbotham's Monte Carlo code [Hi98]. With the standard parameters and $n = 1.015$ one gets 6 photoelectrons. This results in a detection efficiency of $> 99\%$ for a 1 p.e. cut and 88% for left-right coincidence of $\geq$ 1p.e. The experience with the Hall A A2 and the HKS prototype suggest that this simulation is a lower estimate. Therefore, it is expected that we will actually see closer to 10 photoelectrons and achieve a left-right coincidence efficiency close to 98%.

Focal Plane Polarimeter To measure the ratio of proton electric to magnetic form factor at $Q^2 > 12$ GeV^2 using the recoil polarization technique, the focal plane polarimeter (FPP) which is being built for the HMS will have to be moved to the SHMS. The FPP is in effect two polarimeters in series, so there is a CH_2 analyzer followed by drift chambers and then an additional CH_2 analyzer followed by drift chambers. A drawing of where the FPP would fit into the SHMS detector package is shown in Fig. 212. The 2nd Čerenkov and aerogel/TRD would have to be removed.

Trigger, Data Acquisition, and On-line Computing

Trigger The focal plane trigger electronics used for the HMS and SOS has been designed to be flexible, fast and efficient at detecting particles. These triggers consist of requiring hits in a majority of the hodoscope planes combined with options to require or veto on signals from the various particle ID capable detectors in the focal plane hut. The SHMS trigger electronics will be

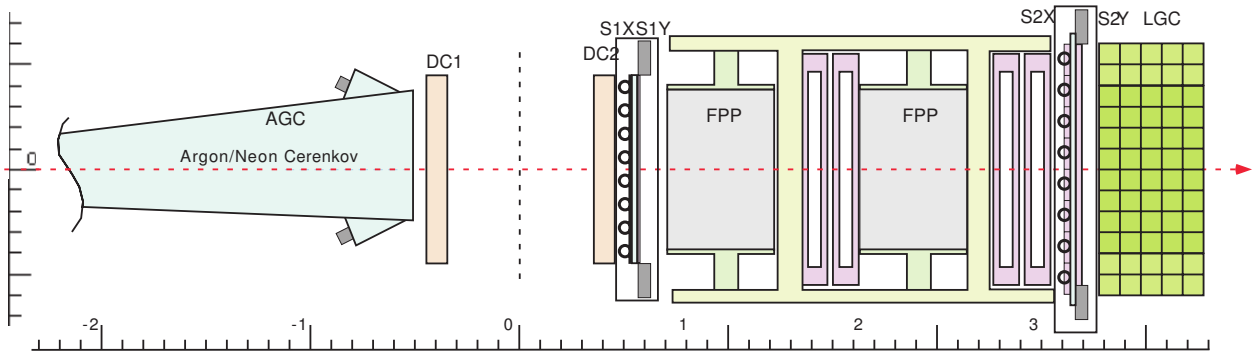

Figure 212: A Schematic of where the Focal Plane Polarimeter could fit into the SHMS Detector Package. There are two CH_2 analyzers, each followed by a set of drift chambers.

similar to the HMS and SOS logic but there will be opportunities for increased sophistication in the trigger.

The design of the HMS and SOS triggers was in part driven by the desire to minimize the time to form the trigger, thus minimizing the amount of delay required for the TDC and ADC inputs from each PMT. With the use of common stop TDCs and ADCs such as those described below, triggers will not need to be formed as quickly. This will allow for the possibility of more sophisticated triggers and the use of computer controllable logic modules.

DAQ Electronics The fine resolution (0.5 ns) TDCs used for the Hall C drift chambers are multihit common-stop models that do not require long cables to delay the signals until a trigger arrives. The absence of delay cables greatly simplifies the physical layout of the experimental apparatus and electronics and also simplifies the commissioning of experiments. Such common-stop devices have not been available at the higher resolutions required for PMT based detectors, and no similar devices have been affordable for charge digitization. For PMT digitizers the inputs must be delayed by approximately 400 ns to wait for the formation of focal plane triggers and a coincidence between spectrometers. Recent advances, however, make it clear that multihit, buffered, common stop TDCs and ADCs of sufficient resolution will be available for the SHMS.

The JLab Physics Electronics Group is developing a 64/32 channel TDC based on the F1 chip [Br99a]. When used in the 32 channel mode this TDC will have a least count of 60ps, yielding sufficient time resolution for any PMT based detector. The effort to develop this TDC is already well advanced and it is expected that the VME module being developed will be used by some experiments at JLab within the next few years. The per-channel cost of this TDC is expected to be comparable to that of common-start high-resolution TDCs used now.

Standard ADCs operate by integrating the current on an input while a gate is present. Since this gate is generated by a trigger which can take many hundreds of nanoseconds to form, each ADC input must be delayed with long coaxial cables. The use of analog delay can be avoided by using a Flash ADC to continuously digitize the input and saving the data in memory while waiting

for the gate. When the gate arrives, the appropriate samples can be summed to produce a digital integration of the input. While this technique has been used, it is not in common use for situations with PMT pulses only a few tens of nanoseconds in width.

While affordable commercial Flash ADC modules are not available, indications are that either affordable modules will be available before the upgrade or that building suitable modules at JLab will be feasible. Flash ADC modules suitable for particle physics use, such as the Struck SIS3300, are available now. This 8 channel module which digitizes at 100MHz with a 12 bit Flash ADC would work well with detectors with wide PMT pulse shapes. However, the cost per channel is several times that of conventional ADCs, so the module would only be appropriate for prototyping and specialized applications.

As part of R&D efforts for the Hall D GlueX experiment, a single channel ADC prototype that uses a 250MHz 8bit Flash ADC chip has been designed. The key components of this design are inexpensive, so overall costs should be comparable to those of conventional ADC modules. Even though the 8 bit resolution is less than the 10 to 14 bits typically used in nuclear physics spectrometers, some resolution is recovered by the fact that a PMT pulse a few tens of nanoseconds wide will be sampled several times yielding better precision. An ADC based on this existing design is already good enough for the majority of the charge digitization required for the SHMS, but we note that higher resolution flash ADCs may be affordable at the time of the upgrade. The JLab electronics group is currently exploring development of a general purpose ADC module based on the GlueX flash ADC prototype.

A side-benefit of flash ADCs is that not only do they record pulse shape, but also pulse timing. Although it is unlikely that a flash ADC can obtain time resolutions as good as the 60ps of the F1TDC, sub nanosecond timing is feasible. This will allow moderate time resolution to be obtained for detectors such as Gas Čerenkov, Aerogel, TRD, and Lead Glass shower counters without additional discriminators or TDC modules.

Data Acquisition and On-line Software The philosophy of the data-acquisition system for Hall C with the SHMS is that the DAQ should not be the limiting factor in the event rates that can be handled. Experience in Hall C has shown that factors other than DAQ, such as accidentals rates or singles rates on individual detectors, generally limit overall trigger rates to less than 10K events/s. With the front end TDC and ADC electronics discussed above, a DAQ system can be constructed that can handle event rates in excess of 10K/s with minimal deadtime. Other than the front end electronics, no technology advances are required in order to obtain these data rates. Future improvements in the speed and cost of networking, CPUs, and disk drives will only help to simplify the design of the DAQ system.

Data acquisition will continue to be managed by CODA[CODA]. CODA development over the next few years will include an emphasis on an on-line analysis farm as a part of CODA. With the upgrade we plan to add a moderate analysis farm. This will have two uses:

1. Real-time accumulation of diagnostic histograms

2. Data compression (background filtering, sparsification)

Stand-Alone (Third-Arm) Calorimeter A large lead-glass calorimeter is planned to be used in experiments in Hall C with the present CEBAF 6 GeV machine. An approved experiment, GEP-III, will use the calorimeter to detect the scattered electron from the elastic $\vec{e}p$ reaction. This experiment will measure the ratio of proton electric to magnetic form factor at $Q^2 = 9$ GeV^2 by measuring the ratio of the transverse to longitudinal polarization of the outgoing proton in the elastic $\vec{e}p$ reaction. To cleanly identify elastic events, the scattered electron will be detected in a lead-glass calorimeter. This calorimeter is being constructed and is expected to be ready for the GEP-III experiment in 2005. The new calorimeter can be used in experiments to measure the ratio of proton electric and magnetic form factors at $Q^2 = 9$–14 GeV^2, and to perform $\gamma - \pi^\circ$ production experiments. This new calorimeter is also planned to be used in real Compton scattering (RCS) experiments with 11 GeV beam energy which are extensions of experiments done with 6 GeV beam.

The calorimeter will consist of 1600-1700 lead-glass blocks. Two sizes of lead glass are used in the calorimeter. One set (which was used in the RCS experiment which ran in Hall A) has a frontal area 3.8x3.8 cm with length of 45 cm. The other set has a frontal area of 4.0x4.0 cm with length of 40 cm. The expected position resolution is 3-5 mm. The lead-glass calorimeter will have a frontal area of 2.7 m^2 and an aspect ratio of 2:1. The infrastructure for the calorimeter, such as platforms, cabling, and electronics, is planned to be usable for the experiments with 12 GeV beam. The electronics readout will be flexible. It will use active splitters for amplitude digitization of each channel and timing of the sums of 8 channels. The splitters will be designed to allow the full formation of a calorimeter trigger for experiments that need it, such as the RCS experiments.

3.D Hall D and the GlueX Experiment

3.D.1 Introduction

The goal of the GlueX experiment is to search for gluonic excitations of $q\bar{q}$ pairs with masses up to 2.5 GeV/c^2. The identification of such states requires knowledge of their production mechanism, identification of their quantum numbers, J^{PC}, and measurement of their decay modes. These in turn require a partial wave analysis of exclusive final states. The decay products of produced mesons must be identified and measured with good resolution and with full acceptance in decay angles. In many cases, the decays of mesons involve a chain of particle decays. The GlueX detector must therefore be hermetic (effective 4π coverage) and have the capability of measuring directions and energies of neutral particles (γ, π^0, η) and four-momenta of charged particles with good resolution. Clearly, particle identification is also required.